Università degli Studi del Piemonte Orientale "A. Avogadro"

DIPARTIMENTO DI DI SCIENZE ED INNOVAZIONE TECNOLOGICA
Corso di Dottorato di Ricerca in Scienze Chimiche

XXVI Ciclo di Dottorato

Ab Initio Modelling of Semiconductor Nanoparticles for Optoelectronics and Photovoltaics

Candidato:
Fabio Grassi

Relatore:
Prof. Maurizio Cossi

Anno Accademico 2013-2014

Ai miei genitori Fernando Grassi e Silvia Pagliani, a mio nonno Ugo Pagliani, a mia moglie, Valentina Villani ed ai miei fratelli Luca e Marco Aurelio.

Acknowledgements

I wish to extend my gratitude to Dr. Mario Argeri for his invaluable scientific and moral support and to Prof. Maurizio Cossi for his tutorship.

This work was part of the European Union-funded international projects Innovasol and Globasol.

4

O quam contempta res est homo, nisi supra humana surrexerit!

Lucius Annaeus Seneca

Acronyms and symbols

DSSC: Dye Sensitized Solar Cell
QD: Quantum dot
QDSSC: Quantum Dot Solar Cell
CBS: Chemical Bath Deposition
DFT: Density Functional Theory
LDA: Local Density Approximation
GGA: General Gradient Approximation
STO: Slater Type Orbital
GTO: Gaussian Type Orbital
BSSE: Basis Set Superposition Error
CP: Counterpoise Correction
TMPO: Trimethylphosphine oxide
TOP: Trioctylphosphine
TOPO: Trioctylphosphine oxide

List of Publications

- M. Argeri, M. Cossi, F. Grassi, A. Fraccarollo, L. Marchese; "DFT Modelling of PbSe Nanoclusters: Effect of Surface Passivation on Shape and Composition"; Journal of Physical Chemistry C, 2011, 115, 11382-11389.
- F. Grassi, M. Argeri, L. Marchese, M. Cossi; "A First Principle Study of Capping Energies and Electronic States in Stoichiometric and Non-Stoichiometric PbSe Nanoclusters"; Journal of Physical Chemistry C, 2013, 117, 26396-26404.

Conferences and Schools Attended

- VII Convegno Nazionale Sulla Scienza e Tecnologia dei Materiali, Acicastello, Italy, 26-29 June 2011. Short Oral: "'Theoretical Modelling of PbSe Nanoclusters: Shape, Stoichiometry and Electronic Properties"'.
- XXVII Winter School of Theoretical Chemistry, "'Excited State Properties"', Helsinki, Finland, 12-15 December 2011. Poster: "'DFT-TDDFT Study of Squaraine Adsorption on PbSe Surfaces"'.
- I Congresso Nazionale della Divisione di Chimica Teorica e Computazionale della Società Chimica Italiana, Pisa, Italy, 22-23 February 2012. Poster: "'DFT-TDDFT Study of Squaraine Adsorption on PbSe Surfaces"'.
- International Meeting on Atomic Physics and Chemistry 2012, Pisa, Italy, 12-14 September 2012, Poster: "'A First Principles Study of

Capping Energies and Electronic States in Stoichiometric and Non-Stoichiometric PbSe Nanocrystals"'.

- 48th Symposium on Theoretical Chemistry, Karlsruhe, Germany, 23-27 September 2012. Poster: "'A First Principles Study of Capping Energies and Electronic States in Stoichiometric and Non-Stoichiometric PbSe Nanocrystals"'.

- II Congresso Nazionale della Divisione di Chimica Teorica e Computazionale della Società Chimica Italiana, Padova, Italy 20-22 February 2013, Oral: "'A First Principles Study of Capping Energies and Electronic States in PbSe Nanocrystals"'.

- 3rd International Conference on Semiconductor-Sensitized and Quantum Dot Solar Cells, Granada, Spain, 9-11 June 2013. Oral: "'A First Principles Study of Capping Energies and Electronic States in PbSe Nanocrystals"'.

- 7th International Conference on the Theory of Atomic and Molecular Clusters, Birmingham, United Kingdom, 15-20 September 2013. Poster: "'A DFT Study of PbX (X = S, Se, Te) Nanocrystals: Effects of Stoichiometry and Ligands on Electronic Structure"'.

Contents

List of Tables

Chapter 1

Introduction

> The question at once presented itself as to whether it would be possible to *start a current through the selenium merely by the action of light.*
>
> W. G. Adams, R. E. Day
> Proceedings of the Royal Society of London, 1876

1.1 The Energy Issue

With the global power consumption standing at 546.8 quadrillion BTU in 2013 and expected to rise to 819.6 by 2040 [1], the energy issue stands as one of the main challenges of this age. In 2010, approximately 85% of the energy produced in the world was obtained by combustion of fossil fuels and 5% by nuclear fission (Figure 1.1): the massive use of these sources has caused serious environmental concerns, with

the awareness of the implicit risks associated with the extraction and use of oil, shale gas and uranium rapidly diffusing from the scientific community into the general population, and by 2050, the atmospheric concentration of CO_2 is expected to rise to an alarming 900-1000 ppm [2]. The current dependence on non-renewable energy sources also prompts considerations of an economic and geopolitical nature: with the supply of fossil fuels widely expected to become exhausted within the end of the century [3], oil prices are bound to be subject to a steep increase, while the scarcity and dishomogeneous geographical distribution of uranium make nuclear power a precarious and thus strategically disadvantageous alternative, which also inescapably poses the problem of radioactive waste processing, as well as the issue of its disposal: isotopes generated during fission reactions in power plants have half-lives that extend from hours or days to 10^4, 10^5 and even 10^7 years, making them both a short and long term hazard. All these factors considered, the need for an affordable and environmentally sustainable energy source is now evident at all levels of society and elicits a concerted political, economic and scientific effort to develop safe and efficient technologies capable of addressing the problem of power sources. In this context, photovoltaic devices stand as one of the most promising candidates for providing a clean and affordable solution for the energy issue.

1.2 Photovoltaics

The photovoltaic effect, that is, the production of an electric current by absorption of electromagnetic radiation, has been known since 1839, when Becquerel first reported the generation of electric current when AgCl coated Pt electrodes were immersed in an electrolyte solution that was exposed to sunlight [4], and the first paper describing a solid state photovoltaic device dates back to 1876 [5]. In almost two centuries, significant scientific and technological advancements have been made and photovoltaics has grown into an independent field of research, as a result of ever growing interest in the subject

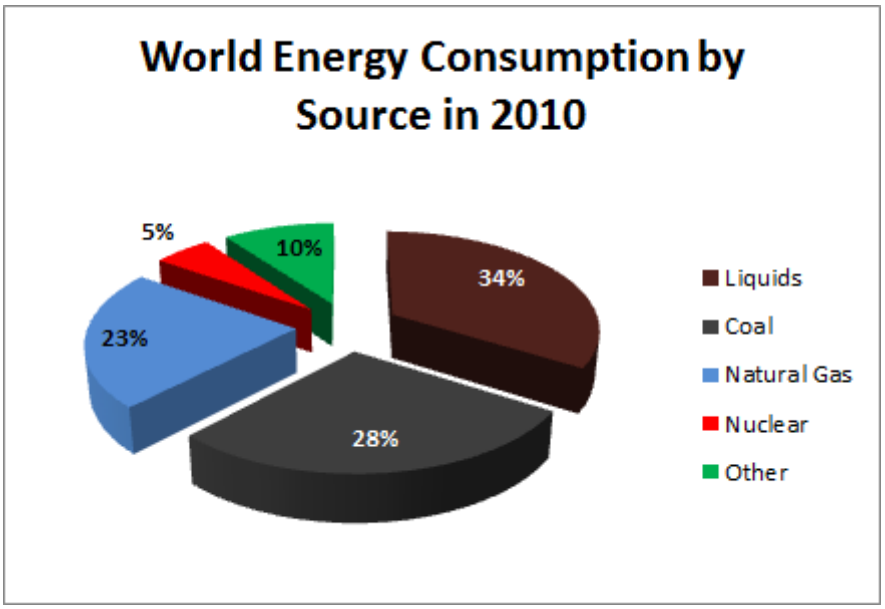

Figure 1.1: Energy sources in 2010: "liquids" includes crude oil, gasoline, diesel, propane, biofuels. "Other" includes hydroelectric, geothermal, photovoltaic, eolic, biomass and ethanol. Source: U.S. Energy Information Administration[1].

caused by this technology's potential: by its very nature, solar power is environmentally friendly, reliable, inexhaustible by any practical timescale and independent of such variables as economic fluctuations and shifting diplomatic scenarios. Solar energy is also extremely abundant: the power that from the Sun reaches Earth's surface is estimated to be approximately 120 PW, which is two orders of magnitude greater than mankind's needs[6]. These qualities make it a very attractive alternative to non-renewable energy sources, however, its virtues notwithstanding, solar power has thus far made a small impact, with only a minor percentage of the energy production obtained with photovoltaic devices. The reasons behind photovoltaic technology's failure to replace other, non-renewable and non-sustainable energy sources are to be sought not only in the economic interests of oil companies and in supply-chain costs [7], but also in its poor affordability: silicon solar cells, the most common type of photovoltaic device, require crystalline silicon, which at present is still a major burden in terms of production costs. Another important limit-

ing factor is the maximum theoretical efficiency, which is famously set by the Shockley-Queisser limit at approximately 30 %, depending on the material band gap [8]. In order to overcome these limitations, several new solutions are being developed: amongst the most promising of these are Dye-Sensitized Solar Cells.

1.3 Dye-Sensitized Solar Cells

First described in Grätzel and O'Regan's seminal paper in 1991 [9], dye-sensitized solar cells (DSSCs) are a very recent type of photovoltaic device. For the purpose of providing a contextual framework, a brief description of these cells is is offered (for two exhaustive studies on this topic, refer to Hagfeldt and coworkers' review [10] or Kalyanasundram's book[11]) and the basic setup of a DSSC is shown in Figure 1.2: on a substrate of conductive glass, a film of wide-bandgap semiconductor (commonly titanium dioxide) is deposited. The structure of the semiconductor is a network of nanocrystals, normally 10-30 nm in diameter and connected by sintering to provide electronic conduction, upon which dye molecules are adsorbed: the nanocrystalline structure of the semiconductor exposes a surface area orders of magnitude greater than its corresponding geometric area, thus allowing for more molecules to be adsorbed. The conductive glass is connected externally to a counterelectrode immersed in a solution of I^-/I_3^- in CH_3CN. Upon absorption of an incident photon of sufficient energy by a dye D (normally a metallorganic Ru complex), an electron-hole pair is generated, with the excitation of an electron to a virtual orbital. The excited electron then relaxes to the bottom of the conduction band of the semiconductor, effectively becoming injected into the nanocrystalline network, at which point recombination with the hole becomes kinetically unfavoured, and an electric current is generated as it percolates through the semiconductor film and travels through the external circuit to reach the counterelectrode, where it is involved in the reduction of a triiodide ion to iodide. The iodide then migrates through

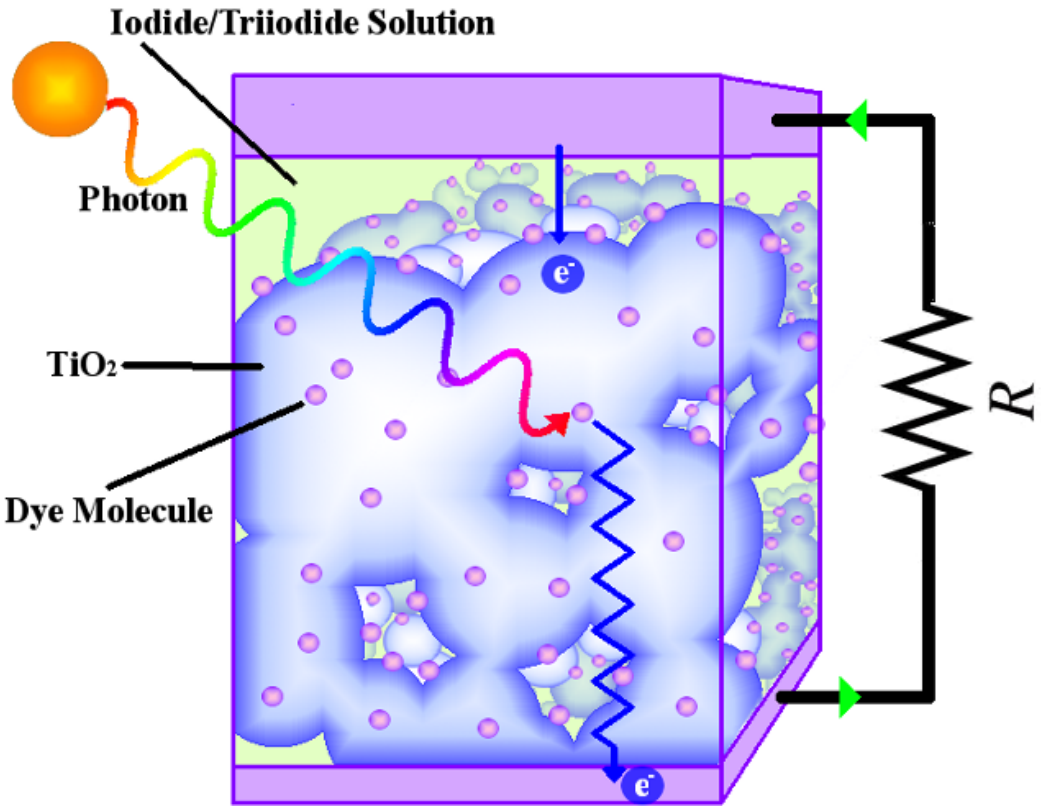

Figure 1.2: Basic schematic representation of a dye-sensitized solar cell.

the solution and reaches D^+, where electron and hole recombine and I^- is oxidised to I_3^-, thus closing the cycle.

1.4 Energy Loss Pathways

DSSCs have attracted considerable attention from both scientists and investors, owing to their advantages: they are lightweight, can be made flexible, can be integrated in architectural design (coloured panels, windows), and perhaps most importantly, they are remarkably cheaper than standard solar panels. Unfortunately, their efficiency is also lower, the current record standing at 15 % [12]. Factors affecting the performance of DSSCs include energy loss pathways such as the reduction of a D^+ from an electron in

the TiO_2 generated at a different site, or direct recombination with an electrolyte, as well as the inability of dyes to absorb radiation at any energy below that of its HOMO-LUMO transition. Another important source of energy loss are so called "'hot carriers"' (Figure 1.3): following adsorption of incident light by the dye molecule, an electron will be excited to either the LUMO or a higher energy virtual orbital, depending on the frequency of the corresponding electromagnetic radiation. Once injected into the TiO_2, the electron will relax nonradiatively to the bottom of the conduction band, releasing the excess energy $\Delta E_l = E_{UMO}$ - E_{CB} (with E_{UMO} and E_{CB} being the energy of the unoccupied molecular orbital in the dye and the bottom of the conduction band of the semiconductor, respectively) as heat. In the case of HOMO-LUMO transitions, this energy loss can be reduced, though never fully removed, by appropriately designing dyes with a small ΔE_l between the LUMO and the bottom of the conduction band. Transitions involving virtual orbitals other than the LUMO will however imply greater energy losses: a significant portion of the energy of photons with an energy greater than that corresponding to the HOMO-LUMO transition will therefore be lost. This is one of the main contributions to the Shockley-Queisser limit. It is important to note that the hot carrier energy loss is not DSSC-specific but is a significant limiting factor in all p-n junction-type photovoltaic devices. In order to increase the efficiency of solar cells, it is necessary to recover some of the energy lost as heat or due to recombination in one of the competing mechanisms. One possible way to do this would be to exploit a phenomenon known as Impact Ionization, a process by virtue of which a single incident photon generates two or more e^-/h^+ couples that has been observed in bulk semiconductors since the 1950's [13, 14]: in theory, this property could allow to obtain quantum yields greater than 100%, thus boosting the efficiency well over the Shockley-Queisser limit. In practice however, Impact Ionization is very inefficient in bulk semiconductors.

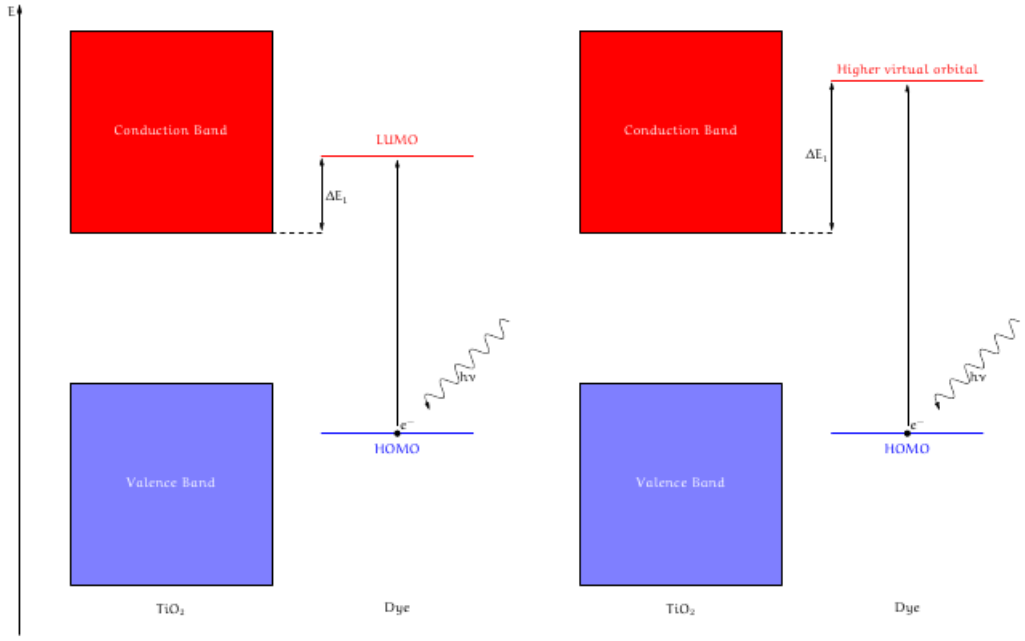

Figure 1.3: Energy level diagram of the energy loss ΔE_l in DSSCs due to the difference between the virtual orbitals in the dye and the bottom of the TiO_2 conduction band.

1.5 Quantum Dots

1.5.1 General Properties

In the early 2000s, a possible route to recover part of the energy of hot carriers has been identified in semiconductor quantum dots (QDs). QDs are a recently discovered class of materials which are defined as having dimensions comparable to that of the first exciton bohr radius. First reported in the 1980s [15, 16], they have become the object of intense scientific interest as a consequence of the possibility to fine-tune their properties, which are markedly size dependent, due to the confinement of the movement of electrons (quantum size effect, Figure 1.4): as the size of the particle decreases from macroscopic to nanometric, energy levels of the orbitals change drastically from the common band structure found in solids to molecule-like discrete levels and the band gap (or HOMO-LUMO gap) increases. One evident result of this property is the possibility to synthesize QDs of the same material capable of absorbing light at different wavelengths simply by altering their size. Very recently, a process similar to Impact Ionization has been reported in quantum dots[17, 18]: following absorption of an incident photon of $E > 2E_g$, with E_g being the quantum dot band gap, the generation of multiple excitons, the bound state of an electron and hole, is observed (Figure 1.5). Contrary to what happens in bulk semiconductors, the process is competitive with phonon emission: in quantum confined systems the energy gap between different levels is significantly greater than phonon energies and therefore, for the energy conservation principle to be satisfied, the excess energy of hot carriers can only be dissipated through unlikely multi-phonon processes [19]. Though conceptually very similar to Impact Ionization, this phenomenon has been given the name Multiple Exciton Generation, to emphasize the bound state of the electron-hole pair within the QD [19]. The possibility of effectively recovering some of the energy of hot carriers and thus to overcome the Shockley-Queisser limit has sparked great interest in the potential application of semiconductor quantum dots in photovoltaics.

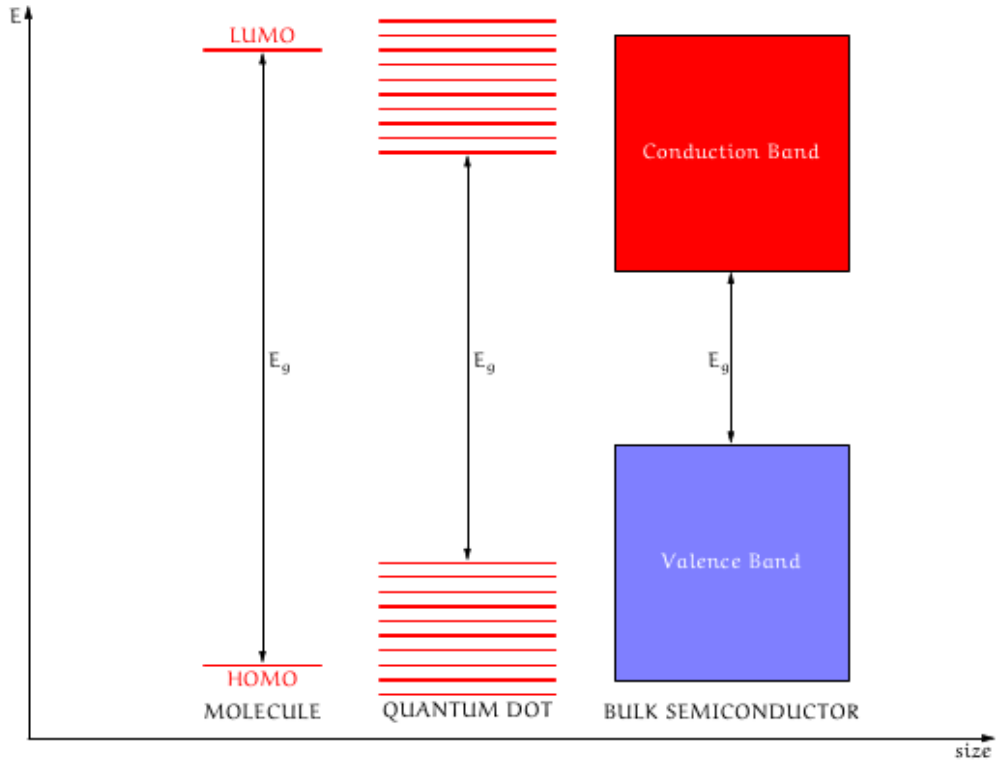

Figure 1.4: Electronic structure transitions from bands to discrete levels and the band gap increases, as particle size decreases.

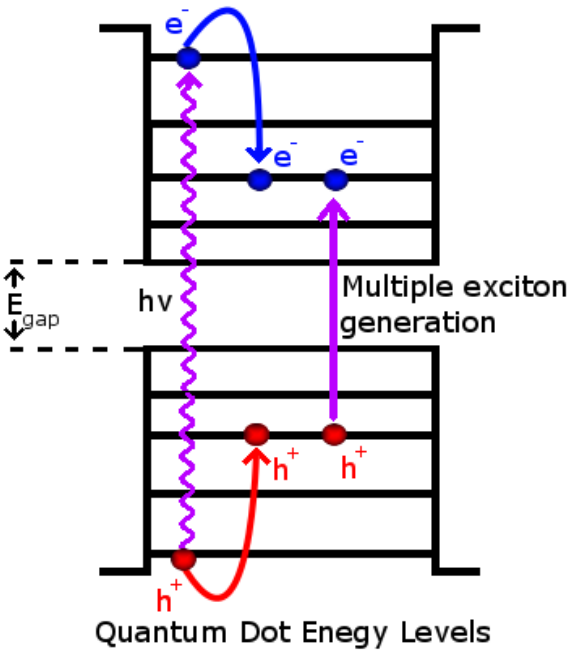

Figure 1.5: Energy level diagram of multiple exciton generation. Filled blue circles: electrons; empty blue circles: holes.

1.5.2 Applications

Since the first reports of successful syntheses, remarkabe progress has been made in understanding and controlling the physico-chemical factors that govern the properties of QDs: the group of Alivisatos, which has been active in perfecting synthetic routes, has successfully obtained colloidal PbSe QDs of diameter as small as 1 nm, while also achieving size distributions of under 2 nm[50]. As the exciton Bohr radius for PbSe is 46 nm[51], such precise control over QD size allows for a comparatively vast range of sizes in the quantum confined regime which lend themselves to many potential applications: quantum dots have been employed in a vast range of fields, spanning from medical imaging[20, 21] to quantum computing[22], photovoltaics and optoelectronics, the latter two being particularly relevant to this study. Though a detailed description of all applications would be beyond the scope of this work (interested readers may refer to the reviews by Kramer and Sargent[54, 55] on the topic of QD photovoltaics and to the review by

Shirasaki and coworkers on QD optoelectronics[23]), a brief summary of the main characteristics of QD solar cells and optoelectronic devices is presented.

Quantum Dot Photovoltaics

QDs have been used alongside molecular dyes in DSSCs since as early as 1996[25] and the earliest report of a photovoltaic device in which semiconductor QDs were the primary absorber was published in 1998[26]. Multiconfigurational ab-initio studies by Prezhdo and coworkers have shown that a non-neutral charge, either positive or negative, has a quenching effect on MEG[52] and also demonstrated that MEG in PbSe QDs can occur upon the absorption of single photons and does not require unlikely two-photon processes [53], while in a DFT and molecular dynamics study they found that band gap tends to increase linearly with both temperature and pressure. Several Colloidal Quantum Dot (CQD) cell architectures are currently being researched, and a detailed description and comparison of all varieties would be beyond the scope of this work (interested readers may refer to the reviews by Kramer and Sargent[54, 55] on this topic); as an example, the structure of CQD-Sensitized Solar Cells, two of the earliest types developed, is presented. Following the basic scheme of DSSCs outlined in Section 1.3, a nanocrystalline wide band-gap semiconductor, often TiO_2, is deposited on conductive glass and connected externally to a counterelectrode that dips in a solution in which a hole carrier, such as I_3^-, is dissolved. Anchored to the wide band-gap semiconductor are the CQDs, which act as light harvesters and can be attached to the surface either by direct contact or using a binfunctional linker, with the latter option in particular having been shown to enable greater coverage of the semiconductor surface [27]. Upon absorption of a photon by a quantum dot, an excited electron is injected into the TiO_2 and percolates through the nanocrystalline network and to the conductive glass. After exiting the cell thorugh an electric contact, it performs electrical work and reaches the counterelectrode, where it reduces the I_3^- to I^-, which in turn migrates through the solution and eventually restores the QD

to its neutral state, thereby becoming reoxidized to I_3^- and closing the cycle. Though very promising in principle, practical attempts to exploit quantum dots for solar cells have thus far found limited success: the best performing device reported to date has an efficiency of 7.0 % [28], and though progress is going at a promising pace, with the record efficiency having almost doubled in less than five years, this performance is still too low to make QD photovoltaic technology a viable alternative. Part of the reason for the low efficiency of QD cells is to be sought in the peculiar electronic structure of QDs, which often features electronic states, often referred to in litrerature as surface states or trap states, that significantly affect MEG and charge transfer [29, 30]. The surface of QDs is commonly passivated with molecules of different nature, which can become adsorbed onto their surface either during synthesis or as part of post-synthetic treatment: ligands play an important part in the behaviour of these systems and their role in the morphology and electronic properties of QDs will be further elucidated in this work.

1.5.3 Optoelectronics

Many of the properties that make semiconductor quantum dots particularly appealing for photovoltaic applications have also attracted attention in the field of optoelectronics: the possibility to regulate the absorption and emission spectra, coupled with comparatively low manufacturing costs and low power consumption, have made QDs an ideal candidate in applications such as photodetectors, lasers and displays. Quantum confined structures have been used in laser devices from as early as 1982 [31], and since the early days of their development, their advantages have been evident: not only do these devices offer high temperature stability, a property that is especially useful in telecommunications lasers, their power consumption is also comparatively low[32], thanks to very low threshold current densities[33]. Another optoelectronic application in which semiconductor QDs have been successfully employed is infrared photodetectors (QDIPs): the possibility to integrate quantum dots of different size allow for multi-wavelength de-

tection and reduced thermal generation of electrons, which results in increased signal to noise (S/N) ratio and thus better performance. Recently, another improvement over conventional photodetectors has been obtained by exploiting MEG[35], which could allow to increase the S/N ratio even further. Semiconductor quantum dots have also been used in light emitting diodes (LEDs)[36, 37]: significant progress has been made since they were first employed in LEDs, with external quantum efficiency having increased from less than 0.01% to 18% since the first reports twenty years ago [23]. An important advantage of QDs as light sources is the very narrow full-width half-maximum (FWHM) spectral emission. There exist several types of QD LEDs, which are classified based on their charge transport layers: at present, the best performing QD LEDs are those with hybrid organic-inorganic charge transport layers, in which a QD film is in contact with a metal oxide on one side and an organic semiconductor on the other. Quantum Dots have also been proposed for the production of displays, which are expected to create "new industries, products and jobs in science and industry"[34] and, indeed, the first commercial television set based on QD technology has been introduced in the market in the spring of 2013[38].

Chapter 2

Theory

> Philosophy is written in this immense book constantly before our eyes (I am saying the Universe), but it may not be understood if first one does not learn to comprehend its language, and to know the characters in which it is written.
>
> Galileo Galilei
> Il Saggiatore

2.1 The Schrödinger Equation

Most ab-initio methods for the theoretical study of polyatomic systems are based on the time-independent form of the famous Schrödinger equation:

$$\hat{H}\Psi = E\Psi \tag{2.1}$$

with Ψ being the wavefunction of the system, E the energy and $\hat{H}$ the Hamiltonian operator, which is defined as

$$\hat{H} = \hat{T} + \hat{V} \tag{2.2}$$

$\hat{T}$ and $\hat{V}$ being the kinetic and potential energy operators, respectively. In atomic units, the kinetic energy operator is defined as:

$$\hat{T} = \sum_{j=1}^{o} \frac{-1}{2}\nabla_j^2 + \sum_{k=1}^{n} \frac{1}{2m_k}\nabla_k^2 \tag{2.3}$$

where j and k indicize electrons and nuclei, respectively, o and n are respectively the number of electrons and nuclei, ∇_j^2 and ∇_k^2 are the second derivatives with respect to the x, y and z coordintes of the j^{th} and k^{th} nucleus and m_k is the mass of the k^{th} nucleus.

The kinetic energy operator in the absence of external electric or magnetic fields is defined as

$$\hat{V} = \frac{1}{2}\sum_{i,j}{}' \frac{1}{r_{i,j}} - \frac{1}{2}\sum_{j,k} \frac{Z_k}{r_{j,k}} + \frac{1}{2}\sum_{k,l}{}' \frac{Z_k Z_l}{r_{kl}} \tag{2.4}$$

with i and j being the electron indices, k and i nuclei indices, Z_k the charge of the k^{th} nucleus, e the fundamental electric charge and r the distance between two particles. Substituting for 2.4 and 2.3 in 2.2 the extended form of the Hamiltonian is obtained:

$$\hat{H} = \sum_{j=1}^{o} \frac{-1}{2}\nabla_j^2 + \sum_{k=1}^{n} \frac{-1}{2m_k}\nabla_k^2 + \frac{1}{2}\sum_{i,j}{}' \frac{1}{r_{i,j}} - \frac{1}{2}\sum_{j,k} \frac{Z_k}{r_{j,k}} + \frac{1}{2}\sum_{k,l}{}' \frac{Z_k Z_l}{r_{kl}} \quad (2.5)$$

2.2 The Born-Oppenheimer Approximation

In a polyelectronic system, the Schrödinger Equation cannot be solved analytically and it therefore becomes necessary to make certain approximations: in this context, the Born-Oppenheimer approximation plays a central role in Computational Chemistry. The Born-Oppenheimer approximation involves the separation of the movement of electrons and nuclei, thus redefining the wavefunction as the product of two functions:

$$\Psi(q, Q) = \psi(q\|Q)\phi(Q) \quad (2.6)$$

with q and Q being the set of electronic and nuclear coordinates, respectively, $\Psi(q, Q)$ the wavefunction, $\psi(q\|Q)$ a function of q depending parametrically on Q and $\phi(Q)$ a function of nuclear coordinates. Functions $\psi(q\|Q)$ are eigenfunctions of the electronci Hamiltonian H_{el}:

$$\hat{H}_{el}\psi(q\|Q)_k = E_k(Q)\psi(q\|Q)_k \quad (2.7)$$

where k is the index of the eigenfunctions, and the respective eigenvalues, of $\hat{H}_{el}$:

$$\hat{H}_{el} = \sum_{j=1}^{o} \frac{-1}{2}\nabla_j^2 + \frac{1}{2}\sum_{i,j}{}' \frac{1}{r_{i,j}} - \frac{1}{2}\sum_{j,k} \frac{Z_k}{r_{j,k}} = \sum_{j=1}^{o} \hat{h} + \frac{1}{2}\sum_{i,j}{}' \frac{1}{r_{i,j}}. \quad (2.8)$$

It should be noted that any change of Q will result in a change of H_{el} as well and, consequently, of $E_k(Q)$. It is now necessary to define functions $\phi(Q)$: these are eigenfunctions of $(\hat{T}_n + E_k(Q))$, with $\hat{T}_n$ as the nuclear kinetic energy operator. $\hat{T}(Q)$ is proportional to $\frac{\partial^2}{\partial Q^2}$: in the context of the Born-Oppenheimer approximation, integrals relative to $\frac{\partial^2}{\partial Q^2}$ are discarded.

2.3 The Wavefunction

An exact definition of the wavefunction is:

$$\Psi = \sum_i c_i \psi_i \tag{2.9}$$

where the ψs make up a complete base and the cs are numerical coefficients that weigh each base functions. Though mathematically correct, this definition is of little practical value for the purpose of solving the Schrödinger equation. In 1928, physicist Douglas Hartree proposed to address this problem by defining the wavefunction as a product of functions:

$$\Psi = \prod_{i=1}^{n} \phi_i \tag{2.10}$$

where functions ϕ are the molecular spinorbitals and n is the number of electrons. It quickly became evident though how this definition was not consistent with the Pauli Exclusion Principle, a mathematical requirement of which is the antisymmetricity of the wavefunction with respect to the exchange of two electrons. An antisymmetric definition of the wavefunction was later introduced by John Slater:

$$\Phi_S = \frac{1}{\sqrt{N!}} \begin{vmatrix} \phi_1(\vec{X_1}) & \phi_1(\vec{X_2}) & \dots & \phi_1(\vec{X_n}) \\ \phi_2(\vec{X_1}) & \phi_2(\vec{X_2}) & \dots & \phi_2(\vec{X_n}) \\ \vdots & \vdots & \ddots & \vdots \\ \phi_n(\vec{X_2}) & \phi_n(\vec{X_2}) & \dots & \phi_n(\vec{X_n}) \end{vmatrix} \tag{2.11}$$

where $\{\vec{X_i}\}$ is the set of spatial and spin coordinates of the wavefunction. This function is called the Slater Determiant. It is important to observe that in this definition, a significant approximation is implicit: by expressing Ψ as a product of functions, electronic repulsion is treated for each electron as the interaction with an average spherical potential of all other n-1 electrons.

It is now necessary to define ϕs. These are defined as a linear combination of hydrogen-like atomic orbitals, centered on the nuclei, similarly to what was observed in the wavefunction Ψ in 2.9:

$$\phi_i = \sum_i c_i \chi_i \tag{2.12}$$

again, c_i is a numerical coefficient that weighs the contribution of the ith orbital, χ_i.

It must be considered that a wavefunction is required to satisfy certain mathematical conditions imposed by its physical meaning. One such requirement is set by the Born Interpretation, which states that:

$$\iiint |\Psi|^2 dxdydz = 1 \tag{2.13}$$

this interpretation assigns to the square modulus of the wavefunction the meaning of probability density, implicitly restricting the set of possible functions to finite functions. Recalling the form of the kinetic energy operator

as expressed in 2.3, it becomes evident that the wavefunction also needs to be continuous and doubly derivable, due to the presence of the ∇^2 operator.

2.4 The Hartree-Fock Method

One of the first techniques developed to solve the Schrödinger Equation is the Hartree-Fock method. This procedure is based on the Variational Theorem, which guarantees that by applying the Hamiltonian operator to any arbitrary trial function Φ, the relative energy eigenvalue E will always be greater than the energy of the ground state E_0, or equal to E_0 if $\Phi = \Psi$. An important consequence of this theorem is that in order to find the best approximation for Ψ it is sufficient to minimize the energy with respect to Φ.

An important part of the Hartree-Fock method is the Fock operator, $\hat{F}$:

$$\hat{F} = \hat{h} + \hat{J} - \hat{K} \tag{2.14}$$

where $\hat{J}$ is the Coulomb operator and $\hat{K}$ is the exchange operator:

$$\hat{J} = \sum_i \hat{J}_i = \sum_i \sum_{j \neq i} \int \phi_j^*(\vec{x_j}) \frac{1}{r_{ij}} \phi_j(\vec{x_j}) \phi_i(\vec{x_i}) d\vec{x_j} \tag{2.15}$$

$$\hat{K} = \sum_i \hat{K}_i = \sum_i \sum_{j \neq i} \int \phi_j^*(\vec{x_j}) \frac{1}{r_{ij}} \phi_i(\vec{x_j}) \phi_j(\vec{x_i}) d\vec{x_j} \tag{2.16}$$

The Fock operatoris initially built with trial spinorbitals and is then applied to the spinorbitals themselves:

$$\hat{F}\phi_i = \epsilon_i \phi_i \tag{2.17}$$

ϵ_i is minimized on the coefficients of the basis functions χ, iterating the definition of $\hat{F}$ and its application to the spinorbitals, until an arbitrarily defined convergence criterion is met. Spinorbitals thus obtained are then reemployed to generate a new Slater determinant, to which the relevant operators are applied to calculate the observables of interest. The whole process can be expressed in matrix form using the Roothaan equation:

$$\mathbf{FC} = \boldsymbol{\epsilon}\mathbf{SC} \tag{2.18}$$

where $\mathbf{F}$ is the Fock matrix, with elements $F_{ij} = \int \phi_i^*(1)\hat{f}(1)\phi_j(1)d(r_1)$, $\mathbf{C}$ is the basis function coefficients matrix, with c_{ij} as the coefficient of the ith basis function in the expansion of the jth molecular orbital, $\boldsymbol{\epsilon}$ is the diagonal matrix of the energies of the single orbitals and $\mathbf{S}$ is the overlap matrix, with $S_{ij} = \langle \phi_i | \phi_j \rangle$. Expressed in this form, the problem can be solved by diagonalizing the coefficients matrix.

2.5 Density Functional Theory

In 1964, Hohenberg and Kohn proved that all physico-chemical properties of a system can be expressed as a function of its elctronic density $\rho(\vec{x})$, therefore E = E[$\rho(\vec{x})$], and that the Variational Theorem is valid for E[$\rho(\vec{x})$]. To calculate the energy of a system from $\rho(\vec{x})$, Kohn and Sham introduced the equation that was later named after them, which treats electrons as independent of each other and subject to a potential defined in such a way as to make the electronic density of the system equal to that of the ground state,

$$E[\rho(\vec{r})] = T[\rho(\vec{r})] + \int \rho(\vec{r})v(\vec{r}) + E_{ee} \tag{2.19}$$

where $T[\rho(\vec{r})]$ is the electron kinetic energy, $\int \rho(\vec{r})v(\vec{r})$ is the interaction with an external potential and E_{ee} is the electron-electron interaction. The latter is defined as

$$E_{ee}[\rho(\vec{r})] = \frac{1}{2}\int \frac{\rho(\vec{r})\rho(\vec{r'})}{|r-r'|} d\vec{r}d\vec{r'} + E_{XC}[\rho(\vec{r})] \tag{2.20}$$

with $\int \frac{\rho(\vec{r})\rho(\vec{r'})}{|r-r'|} d\vec{r}d\vec{r'}$ as the coulomb interaction between two electrons and $E_{XC}[\rho(\vec{r})]$ which includes exchange and correlation.

Electron densities are calculated by integrating over the molecular orbitals:

$$\rho(\vec{r}) = \sum_i |\phi_i(\vec{r}_i)|^2 \tag{2.21}$$

where each orbital ϕ_i is an eigenfunction of the Kohn-Sham operator:

$$(-\frac{1}{2}\nabla_i^2 + \hat{v}(\boldsymbol{r})_{KS})\phi_i = \epsilon_i\phi_i. \tag{2.22}$$

$\hat{v}(\boldsymbol{r})_{KS}$ is defined as

$$\hat{v}(\boldsymbol{r})_{KS} = -\sum_k \sum_i \frac{Z_k}{r_{ik}} + \sum_i \hat{J}_i + V_{XC} \tag{2.23}$$

with i and k being the electron and nucleus indices, respectively. We have thus introduced V_{XC}, the exchange-correlation potential:

$$V_{XC} = \frac{\delta E_{XC}}{\delta \rho} \tag{2.24}$$

Knowing ρ and $E_{XC}[\rho]$, it is now possible to calculate the energy of the ground state. Unfortunately, the exchange-correlation potential of real physical systems is not known. To solve this problem, several techniques have been developed: the treatment of electrons as independent particles allows to include the V_{XC} of a gas of independent electrons, which is known. This way of handling $E_{XC}[\rho]$ is known as the Local Density Approximation (LDA) and it generally gives good results with periodic systems and has therefore been widely employed in solid state physics. This type of functional does not generate reliable results for most systems of chemical interests, as the distrubiotion of the electron density is considerably different from that of the electron gas model. Better results can be obtained by including the density gradient $\nabla\rho(\vec{r})$: these are known as Generalized Gradient Approximation (GGA) functionals. It should be noted that, while there is only one LDA functional, many GGA functionals can be defined, as the function that describes the electron density gradient is defined arbitrarily: it can be designed to accurately describe the asymptotic properties of a system, ensuring that the energy of two fragments at infinte distance from each other is the same as the energy of the bound fragments, or empirically, by fitting a set of experimental data. A further development of GGA functionals is the inclusion of part of the Hartree-Fock exchange $\hat{K}$, defined using the eigenfunctions of the Kohn-Sham operator:

$$v_{xc}[\rho] = (1-\alpha)v_x + \alpha\hat{K} + v_c[\rho] \tag{2.25}$$

where v_x is the exchange potential and $v_c[\rho]$ is the correlation potential. Functionals of this type are called hybrid. An example of such a functional is the popular B3-LYP, in which 25% of Hartree-Fock exchange is used.

2.6 van der Waals forces and Grimme's Dispersion Corrections

Though DFT has proven to be a reliable tool for the computation of many properties in a wide range of systems, certain quantities of significant interest are still beyond its reach, in no small part due to the approximations implicit in non-exact density functionals. One such case is the calculation of van der Waals forces, for which LDA and its successors provide notoriously unreliable descriptions, as these functionals consider only local properties and are unable to account for instantaneous density fluctuations. One way to circumvent this problem is to add a correction term to the total DFT energy:

$$E_{DFT-D} = E_{DFT} + E_{disp} \tag{2.26}$$

where E_{DFT-D} is the dispersion-corrected total energy and E_{DFT} is the usual DFT energy. E_{disp} is a correction term, itself the sum of a two- and three-body term:

$$E_{disp} = E^{(2)} + E^{(3)}. \tag{2.27}$$

$E^{(2)}$ is the two-body term, and is defined as:

$$E^{(2)} = \sum_{AB} \sum_{n=6,8,10...} s_n \frac{C_n^{AB}}{r_{AB}^n} f_{d,n}(r_{AB}) \tag{2.28}$$

where C_n^{AB} is the averaged nth order (n = 6, 8, 10...) dispersion coefficient for atom pair AB, r_{AB} is the internuclear distance, s_n is a global scaling factor that depends on the density functional used and $f_{d,n}(r_{AB})$ is a damping function used to prevent the dispersion correction from diverging for small values of R_{AB}:

$$f_{d,n}(r_{AB}) = \frac{1}{1 + 6(r_{AB}/(S_{r,n}R_0^{AB}))^{-\alpha_n}}, \tag{2.29}$$

with α_n being a steepness parameter, set to 14 for n = 6 and $\alpha_n + 2 = \alpha_n + 2$ for other values of n, designed to make the dispersion correction $<$

1% of max($|E_{disp}|$) and $s_{r,n}$ the scaling factor of the cutoff radii R_0^{AB}. The dispersion coefficients are obtained from time-dependent DFT calculations (for a more detailed description, see Grimme's paper[39]). The three-body term is defined as

$$E^{(3)} = \sum_{ABC} f_{d,(3)}(\bar{r}_{ABC}) E^{ABC} \tag{2.30}$$

with the sum being over all atom triples ABC, $f_{d,(3)}$ is the damping function defined in Eq. 2.29 ($\alpha = 16$, $s_r = 4/3$), $\bar{r}_{ABC}$ is are geometrically averaged radii, and E^{ABC} is the dispersion term derived from third-order perturbation theory:

$$E^{ABC} = \frac{C_9^{ABC}(3cos\theta_a cos\theta_b cos\theta_c + 1)}{(r_{AB} r_{BC} r_{AC}^3)} \tag{2.31}$$

where θ_a, θ_b and θ_c are the internal angles of the triangle defined by atoms A, B, C, r_{AB}, r_{BC} and r_{AC} are the interatomic distances and C_9^{ABC} is the triple-dipole constant:

$$C_9^{ABC} = -\sqrt{C_6^{AC} C_6^{AC} C_6^{BC}}. \tag{2.32}$$

2.6.1 DFT and Semiconductor Properties

As previously mentioned, in spite of its many successes, Density Functional Theory is still affected by some issues that call for careful consideration when investigating the properties of a material: one of these is the unsatisfactory performance of many functionals with respect to the prediction of band gaps of many insulators and semiconductors; the well known "band gap problem". In semiconductors in particular, the band gap is often underestimated by LDA and GGA functionals [40]. This obstacle does not imply the impossibility to predict the electronic properties of the systems studied in this work with a satisfactory accuracy, indeed DFT has been successfully used to calculate the band gaps of metal chalcogenide quantum dots of materials such as CdTe[47] (LSDA), PbS[48, 89] (GGA) and perovskites [49] (hybrid) in good agreement with experimental results. A simple way to calculate the

band gap E_{gap} is $E_{gap} = I - A$, where I and A are the ionization potential and electron affinity, respectively. While at Hartree-Fock level Koopmans' theorem[41] states that the negative of the HOMO energy eigenvalue is a good approximation of I, similar attempts to find a direct physical meaning to Kohn-Sham orbital energies[42] are often disputed, and even more so for energies of LUMO and above, and thus A, as DFT is a ground state theory and does not guarantee an accurate description of virtual orbitals. Several works have shown that it is possible to obtain physical information from Kohn-Sham orbitals, though the quality of the results depends largely on the xc functional of choice[43, 44, 45]: the dependence of functional performance on the material calls for particular care when investigating the electronic structure of semiconductors at DFT level, especially in the choice of the density functional.

2.7 Basis Functions

The choice of a set of basis functions that describe atomic orbitals is a fundamental step in the setup of an ab-initio calculation: using a complete basis set, made of infinite functions, would produce the true wavefunction Ψ and the true value of its observables. Obviously this is not possible in practice to use infinite basis functions, so it becomes necessary to use incomplete basis sets, which will result in approximations that will generally be more refined as the numer of basis functions is increased. A basis set must always have at least a number of functions equal to the number of electrons of the system: this is called the minimal basis set. Historically, the first basis functions used were those proposed by Slater, called Slater Type Orbitals (STO), which have the following form:

$$\chi^{STO}_{n,l,m}(r,\theta,\phi) = Nr^{n-1}e^{-\zeta r}Y_{l,m}(\theta,\phi) \tag{2.33}$$

where n, l and m represent the three quantum numbers, N is a normalization factor, r θ and ϕ are polar coordinates and ζ is a constant for each element that accounts for the shielding between electrons. Though these provide a good description of atomic orbitals, in computational practice STOs are seldom used. Much more common are Gaussian Type Orbitals (GTO)

$$\chi^{GTO}_{n,l,m}(r,\theta,\phi) = Nr^{2(n-1)}e^{-\alpha r^2}Y_{l,m}(\theta,\phi) \tag{2.34}$$

their form allows four center integrals to be treated as two center integrals, resulting in reduced computational costs.

2.8 Basis Set Superposition Error

In a system composed of two fragments A and B which form adduct AB, the addition energy could be calculated from the exact energies of the monomers and the adduct:

$$\Delta E = E_{AB} - E_A - E_B. \tag{2.35}$$

Normally, the energy of fragments A and B and adduct AB is unknown and must therefore be calculated, using the methods described earlier in this chapter by assigning basis set a to fragment A and basis set b to fragment B. During the calculation of the energy of the adduct, both basis sets are available to the atoms of each monomer. The presence of extra basis functions leads to an overestimation of the addition energy between the two monomers: the change in energy due to the increase of the basis set involves only the adduct (E_{AB} in eq. 2.35) while terms E_A and E_B are calculated with two smaller basis sets. The resulting difference is called Basis Set Superposition Error (BSSE), and it is removed by applying the Counterpoise Correction[46].

A way to correct this error consists of the calculation of energies of single monomers using both basis sets, with a centered on the positions of atoms in monomer A and b centered on the positions of atoms in monomer B, but without including the other monomer in the calculation (commonly called "ghost functions"). The corrected binding energy between two monomers is thus calculated as:

$$E_a = E_{cl}^{cl}(cl) - E_{cl}^{cl}(c) - E_{cl}^{cl}(l) - E_{cl}^{c}(c) - E_{cl}^{l}(l) + E_{c}^{c}(c) + E_{l}^{l}(l) \qquad (2.36)$$

where each element on the right side of the equation represents the energy of the system specified between brackets (c = cluster, l = ligand, cl = adduct), with the subscript and the apex indicating the geometry in which the calculation was performed (c = isolated cluster geometry, l = isolated ligand geometry, cl = adduct geometry) and the basis set (c = cluster basis set, l = ligand basis set, cl = both basis sets), respectively.

Chapter 3

Methods

> An expert is someone who knows some of the worst mistakes that can be made in his subject, and how to avoid them.
>
> Werner Heisenberg
> Physics and Beyond: Encounters and Conversations

3.1 PbSe Properties

Lead selenide is a semiconducting material that crystallizes in the $Fm\bar{3}m$ group and has a band gap of approximately 0.27 eV at room temperature. It is well known from experimental literature that colloidal quantum dots of PbSe are nanocrystalline and exist in the rock-salt cubic structure [56, 57, 58]: this has been verified experimentally by means of X-ray diffraction spectroscopy for QDs with diameter as small as 2.2 nm [60], while computational studies indicate that even sub-nanometer clusters

exhibit bulk structure, including the minimal Pb_4Se_4[59], which has been successfully used in the past for electronic structure calculations [52]. On the basis of this knowledge, all modelling approaches in this work have involved the extraction of clusters from the bulk structure of PbSe. Unless otherwise stated, all calculations were performed on systems with zero total spin.

3.2 Surface Modelling

The first part of the work was dedicated to the study of the relative stability of the crystallographic planes defined by the first three sets of Miller indices: {100}, {110} and {111}. These surfaces were studied on both finite clusters and periodic slabs. As shown in Figures 3.1 and 3.2, {100}

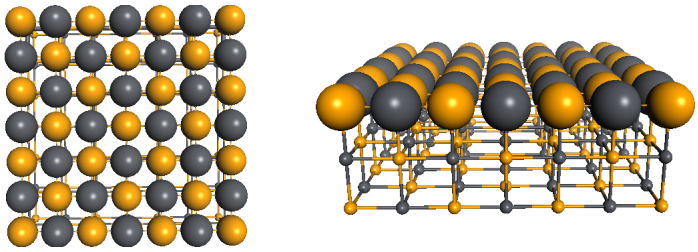

Figure 3.1: Section of {100} plane of PbSe (left: top view, right: side view). Grey spheres: Pb; yellow spheres: Se; large: surface; small: bulk.

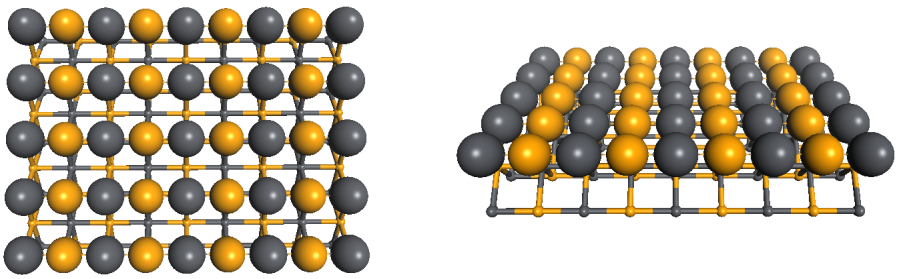

Figure 3.2: Section of {110} surface of PbSe (left: top view, right: side view). Grey spheres: Pb; yellow spheres: Se; large: surface; small: bulk.

and {110}-type faces are stoichiometric, with the former consisting of Pb

and Se atoms, each coordinated by four atoms of the other element with $Pb - \hat{Se} - Pb = Se - \hat{Pb} - Se = 90°$ angles and the latter characterized by alternating parallel lines of Pb and Se atoms. {111}-type faces are non-stoichiometric, exposing either Pb or Se atoms only (Figure 3.3). The clus-

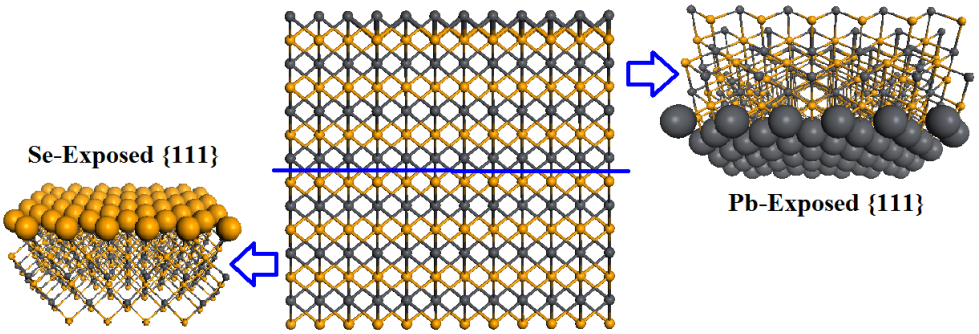

Figure 3.3: Sections of Se-terminated (left) and Pb-terminated (right) {111} planes of PbSe, as cleaved from the bulk (centre). Grey spheres: Pb; yellow spheres: Se; large: surface; small: bulk.

ters used for studying finite sections of the surfaces of interest were cut from the bulk in such a way as to expose one of the three planes and to have the same number of atoms ($Pb_{50}Se_{50}$). Periodic surface modelling was performed by cutting slabs of varying thickness exposing the three planes, with both {111}-type surfaces (Pb- and Se-terminated) considered, and in each case, cleavage energy E_c and surface energy E_s (the energy of the slab primitive cell as cut out of the bulk with respect to the bulk energy, before and after optimization, respectively) were calculated.

The normalized surface energy $\bar{E}$ was also calculated: for {100} and {110} slabs, it is defined as

$$\overline{E} = \frac{E_s}{2A} \tag{3.1}$$

with A being the primitive cell area and E_s the surface energy, which itself is calculated as follows:

$$E_s = E_{slab}^{relaxed} - E_{bulk} \tag{3.2}$$

where $E_{slab}^{relaxed}$ is the total energy of the optimized slab and E_{bulk} is the bulk energy. For {111}-type slabs, a different approach was needed, as surfaces can be either Pb or Se terminated: following the procedure outlined by Fang and coworkers[66], geometry optimization of defective surfaces was performed to obtain {111}-like slabs with one type of face, after which a $2 \times 1 \times 1$ supercell was made from the optimized slab. A Pb layer was then added, resulting in a nonstoichiometric slab exposing two Pb faces, from which half the atoms were finally removed to restore the stoichiometry (Figure 3.4). The procedure was then repeated for Se-terminated {111}-type faces.

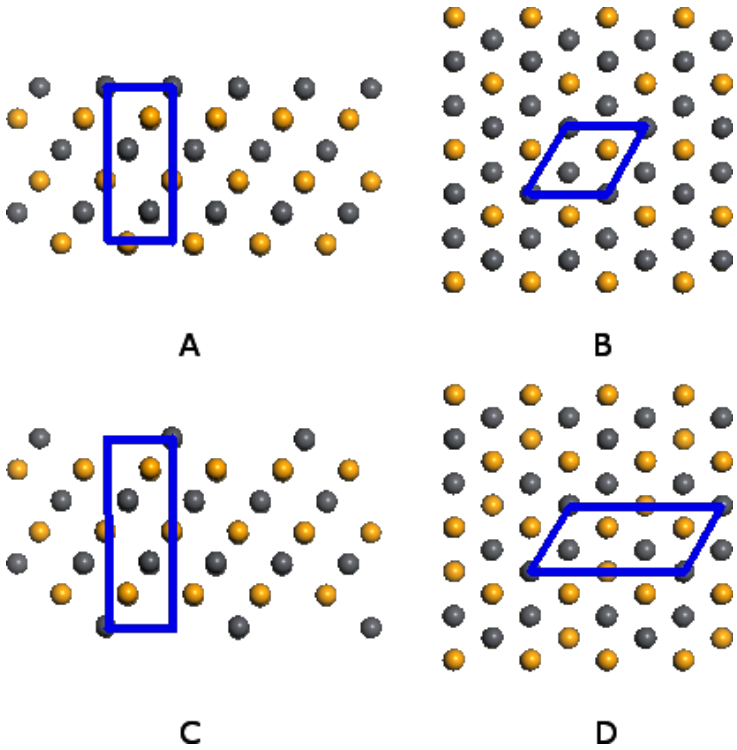

Figure 3.4: {111} PbSe surface modelling. A) Unmodified slab, side view. B) Unmodified slab, top view. C) Modified slab, side view. D) Modified slab, top view. Note how in C and D, the Pb-terminated side is missing half the atoms, which are present on the Se-terminated side, resulting in a cell area that is twice the original size.

3.3 Surface Stability and Ligands

In order to understand the effect of capping molecules on the stability of the surfaces, their interaction with four ligands, trimethylphosphine oxide (TMPO), methylamine (MA), propanoic acid (PA) and propanoate ion (PA^-) was studied (Figure 3.5).

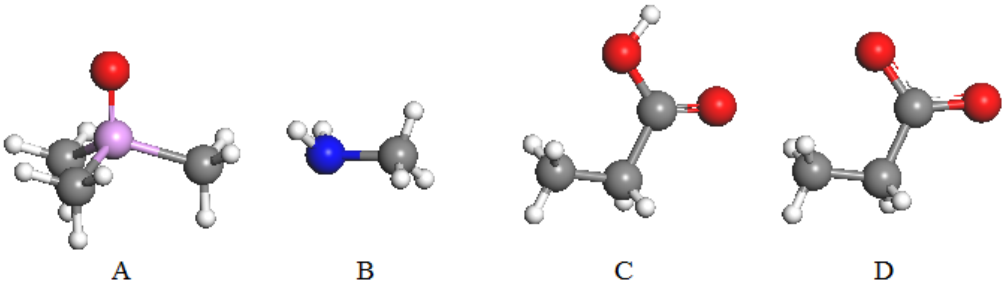

Figure 3.5: Ball and stick representation of the ligands used. A: Trimethylphosphine oxide; B: Methylamine; C: Propanoic Acid; D: Propanoate. Black spheres: carbon; red: oxygen; blue: nitrogen; pink: phosphorus; white: hydrogen.

These were chosen to model trioctylphosphine oxide, alkylamines, oleic acid and oleate, respectively, all of which are present during colloidal nanocrystal synthesis[61, 62, 63] or post synthesis[57]. The interaction was investigated by placing a molecule in the vicinity of the surface of the clusters and slabs described in Section 3.2 and by reoptimizing the structure. Addition energies were then calculated using Formula 2.36, to account for the basis set superposition error and for monomer deformations. The effect of PA^- was only investigated on finite clusters, as its inclusion produced adducts with a net charge of -1, which would result in an infinite charge when replicated with periodic boundary conditions. The effect of capping on the relative stability of PbSe surfaces was studied by taking the clusters and slabs described in the previous section and placing a ligand next to them.

3.4 Cluster Modelling

Based on the results obtained from the study described in Section 3.2, it was decided to concentrate on clusters exposing {100}- and {111}-type surfaces only, as the latter is the most effectively stabilized by capping, while the former has been shown to be the most stable when uncapped[65, 66]. As described in Section 3.2, {111} planes expose only one type of atom, and can be either Pb- or Se-terminated (Figure 3.3). NMR and ICP-MS data clearly show that colloidal PbSe quantum dots feature an outer shell of Pb atoms[63] and an overall Pb:Se > 1 stoichiometric ratio[67, 68]: clusters exposing Se-terminated {111}-type faces were thus discarded, and only Pb-{111} faces were considered in this work.

Clusters of three shapes were modelled: cuboidal, cuboctahedral and octahedral. Cuboidal clusters expose only {100} surfaces and can have formula Pb_xSe_x, $Pb_{x+1}Se_x$ or Pb_xSe_{x+1}: the stoichiometric ratio is 1:1 if the number of atoms on at least one side of the cluster is even, while a stoichiometric excess of one atom occurs when the number of atoms on all sides is odd. Cuboctahedral clusters expose six {100} and eight {111} faces which induce a stoichiometric imbalance. Octahedra expose only {111} faces and are also non-stoichiometric. Thirty-five cuboidal clusters, having formula Pb_xSe_x (x = 4, 6, 8, 10, 12, 15, 16, 18, 20, 24, 25, 27, 30, 32, 36, 40, 45, 48, 50, 54, 60, 72, 75, 90, 108), $Pb_{y+1}Se_y$ and Pb_ySe_{y+1} (y = 13, 22, 37, 62) were extracted from the bulk. These were obtained by cutting cuboids with side length (measured in number of atoms) 2×2×2, 2×2×3, ... 2×2×6, ... 6×6×6. Two clusters of cuboctahedral morphologies were modelled: $Pb_{55}Se_{38}$ and $Pb_{147}Se_{116}$. Lastly, two octahedral clusters, $Pb_{44}Se_{19}$ and $Pb_{85}Se_{44}$, were also studied.

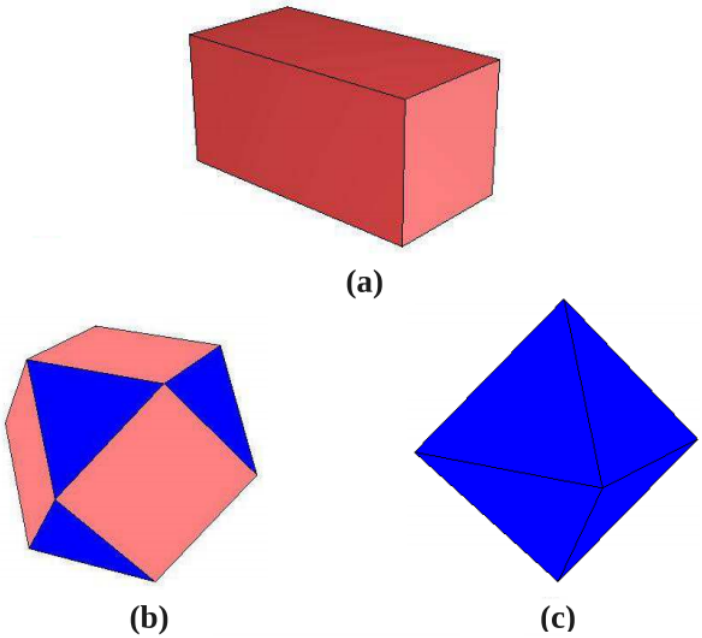

Figure 3.6: PbSe morphologies: a) cuboidal, b) cuboctahedral, c) octahedral. {100} and {111} faces are depicted in pink and blue, respectively.

3.5 Electronic Structure Calculations

In order to investigate the electronic properties of these systems, it was necessary to identify an appropriate computational scheme: while variational methods are known for the reliability of the results on occupied orbitals and their energy eigenvalues, the description of virtual orbitals they provide is not guaranteed to be accurate. An approximate workaround is to artificially induce the occupation of the LUMO, thus variationally optimizing its energy eigenvalue, by imposing a triplet state in the single point calculation. Following the strategy described in a recent paper[88], in which a correlation was observed between the HOMO-LUMO gap and singlet-triplet excitation energies, single point calculations were performed in both singlet and triplet states on the optimized geometries of a subset of the cuboidal clusters described in Section 3.4 using the B3LYP[83] and BLYP [81, 82] functionals and at Hartree-Fock level.

3.6 Morphology and Stoichiometry

One of the aims of this work was to investigate the influence of nanocrystal stoichiometry and morphology on electronic structure. The two variables are not however independent: disregarding defects, cuboidal nanocrystals can only have formula $Pb_{x\pm1}Se_x$ if the number of atoms on all edges is odd, or Pb_xSe_x in all other cases, while clusters exposing {111} surfaces such as cuboctahedra and octahedra are intrinsically non-stoichiometric: the former have formula Pb_xSe_y with coefficients defined by

$$x = \frac{(2n+1)^3+1}{2} - 8\left(\sum_{i=1}^{n}\frac{i(i+1)}{2}\left(\frac{1}{2}(-1)^n - \frac{1}{2}(-1)^i\right)(-1)^n\right) + \\ + \left(-\frac{1}{2} + \frac{1}{2}(-1)^n\right) \tag{3.3}$$

$$y = \frac{(2n+1)^3-1}{2} - 8\left(\sum_{i=1}^{n}\frac{i(i+1)}{2}\left(\frac{1}{2}(-1)^n + \frac{1}{2}(-1)^i\right)(-1)^n\right) + \\ - \left(-\frac{1}{2} + \frac{1}{2}(-1)^n\right) \tag{3.4}$$

with $n \in \mathbb{N}^+$. Demonstration for 3.3 and 3.4 can be easily derived by observing that cuboctahedra featuring only one type of {111} surface can be obtained by cutting eight tetrahedral corners from cubes with k atoms per edge, with k odd, as a cube with an even number of edge atoms would expose both Pb and Se {111} faces. From this consideration, it is possible to calculate the stoichiometric coefficients by subtracting from the total number of atoms for each element the number of atoms of that type in the corners, with each corner consisting of $\frac{k-1}{2}$ sections of {111}-type planes, each being made of $N_a = \frac{l(l+1)}{2}$ atoms, with l being the number of atoms on the side of each triangular section of {111} surface 3.7. It must be noted that the parent cube can have either Pb or Se vertices, depending on the parity of n: this determines the composition of the corners, as with n even, the triangular sections

defined by index i will be made of Pb atoms with i even and Se atoms with i odd, and vice versa for n odd. To account for this alternation, each term of the sum in x was multiplied by a function designed to return 1 when i and n have the same parity and 0 when they have different parity. Likewise, the similar term in y returns 1 when the parity of i and n is different and 0 when it is the same.

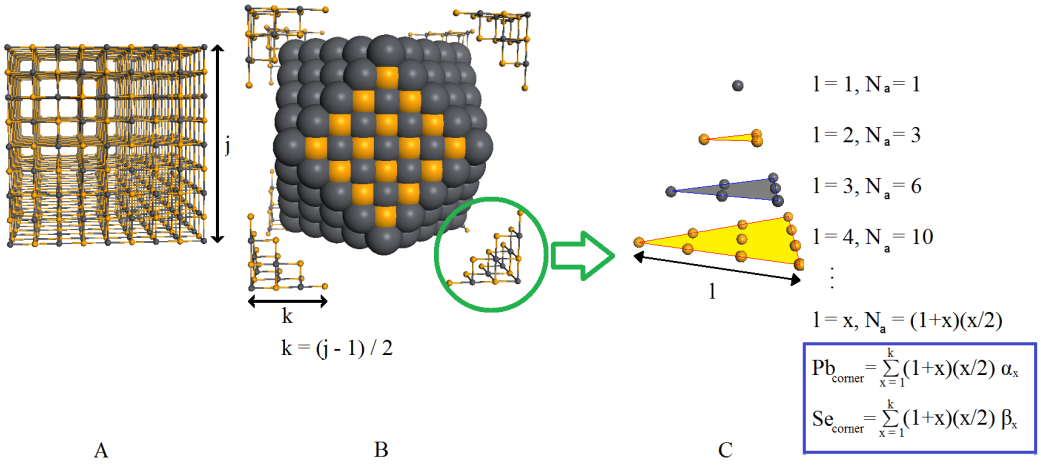

Figure 3.7: A) PbSe cube B) PbSe cuboctahedron obtained by removing eight corners from a cube. C) Composition of one corner removed from a cube showing the parallel triangular Pb (grey) and Se (yellow) sections. α_x and $\beta_x$are coefficients designed to be 0 when x is even and odd, respectively, and 1 in the other case. Cluster stoichiometry can be calculated by subtracting the composition of eight corners from the formula of the parent cube.

Stoichiometric coefficients in octahedra are defined by

$$x = n^2 + 2 \times \left(\sum_{i=1}^{n-1} i^2 \right) \tag{3.5}$$

$$y = (n-1)^2 + 2 \times \left(\sum_{i=1}^{n-2} i^2 \right) \tag{3.6}$$

with $n \in \mathbb{N}^+$. Proof for 3.5 and 3.6 can be derived by noticing that PbSe octahedra exposing {111} surfaces with n edge atoms can be viewed as a

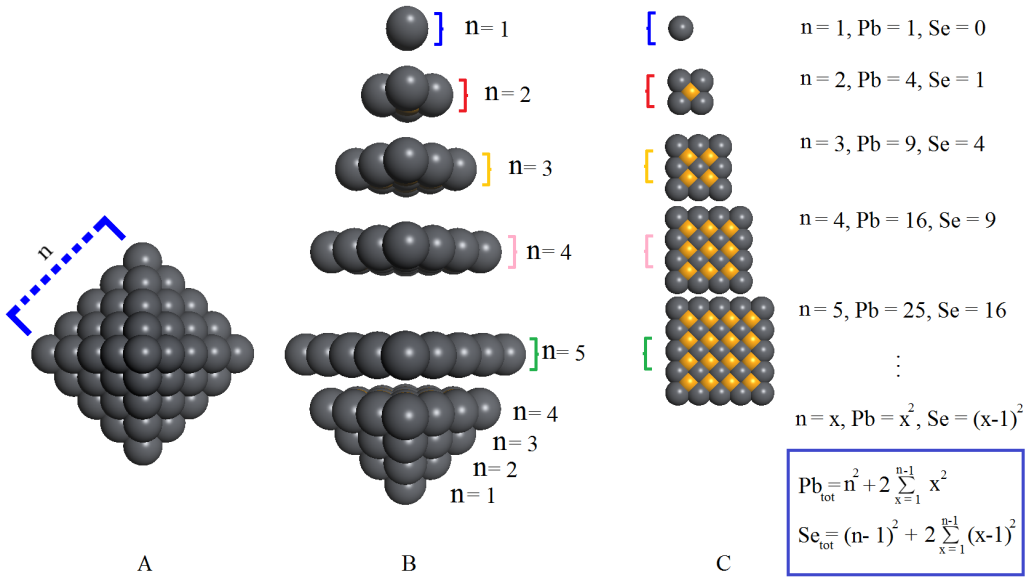

Figure 3.8: A) PbSe octahedron with edge length = n = 5 atoms. B) View of the octahedron as a sequence of stacked parallel square sections. C) Top view and composition of the square sections. Grey spheres: Pb; yellow spheres: Se.

sequence of $2(n-1)$ square sections with formula $Pb_{i^2}Se_{(i-1)^2}$, $1 \leq i < n$, with each value of i defining two equal sections, plus one central square defined by $Pb_{n^2}Se_{(n-1)^2}$ 3.8.

It is easily verified that $x : y \neq 1 \; \forall n \in \mathbb{N}^+$. In order to isolate the effects of morphology and stoichiometry, two different strategies were used: first, a stoichiometric cubic cluster, $Pb_{108}Se_{108}$, was modified by removing one, then two Se atoms from the core, thus artificially introducing a stoichiometric imbalance while leaving the morphology and the exposed surfaces unaltered. The other method used involved a stoichiometric cluster of formula $Pb_{28}Se_{28}$, suitably designed to leave two {111}-type surfaces exposed by removing two opposite corners from a $Pb_{32}Se_{32}$ cube.

PbSe-Formiate Adducts

Cluster	Adsorption Site	Morphology
Pb_4Se_4	Vertex	Cuboidal
Pb_6Se_6	Edge	Cuboidal
Pb_6Se_6	Vertex	Cuboidal
Pb_8Se_8	Edge	Cuboidal
Pb_9Se_9	Face ({100})	Cuboidal
Pb_9Se_9	Edge	Cuboidal
$Pb_{13}Se_{14}$	Edge	Cuboidal
$Pb_{14}Se_{13}$	Face ({100})	Cuboidal
$Pb_{59}Se_{56}$	Face ({111})	Modified cuboidal (Section 3.7)

Table 3.1: PbSe-Formiate adducts: cluster stoichiometry, adsorption site and cluster morphology.

3.7 Effects of Ligands on Electronic Structures

The study of the effect of ligands on electronic properties of PbSe quantum dots was performed by taking a cubic cluster of formula $Pb_{62}Se_{63}$ and removing one corner to leave a section of Pb-terminated {111} surface exposed. The geometry of the resulting cluster, with formula $Pb_{59}Se_{56}$, was then optimized and used for making adducts with $Al(CH_3)_3$, BCl_3, $CH_3CH_2^{\cdot}$, CO, HCOOH, $HCOO^-$, CH_3NH_2, CH_3CH_2SH, PH_3, S atoms and trimethylphophine oxide, which were placed in the vicinity of the {111} surface. The effects of ligands on the electronic structures were then investigated by comparing densities of states.

3.8 Ligand Addition Energy

Addition energies E_a of $HCOO^-$ and CH_3NH_2 were calculated using equation 2.36. Adducts were generated by placing a ligand near face, edge and vertex Pb atoms and optimizing the geometry (Tables 3.1 and 3.2). In some

PbSe-Methylamine Adducts

Cluster	Adsorption Site	Morphology
Pb_4Se_4	Vertex	Cuboidal
Pb_6Se_6	Edge	Cuboidal
Pb_6Se_6	Vertex	Cuboidal
Pb_8Se_8	Edge	Cuboidal
Pb_8Se_8	Vertex	Cuboidal
Pb_9Se_9	Face {100}	Cuboidal
Pb_9Se_9	Edge	Cuboidal
Pb_9Se_9	Vertex	Cuboidal
$Pb_{10}Se_{10}$	Edge	Cuboidal
$Pb_{10}Se_{10}$	Edge	Cuboidal
$Pb_{10}Se_{10}$	Vertex	Cuboidal
$Pb_{12}Se_{12}$	Edge	Cuboidal
$Pb_{12}Se_{12}$	Edge	Cuboidal
$Pb_{12}Se_{12}$	Vertex	Cuboidal
$Pb_{14}Se_{13}$	Face {100}	Cuboidal
$Pb_{14}Se_{13}$	Vertex	Cuboidal
$Pb_{16}Se_{16}$	Face {100}	Cuboidal
$Pb_{16}Se_{16}$	Edge	Cuboidal
$Pb_{16}Se_{16}$	Vertex	Cuboidal
$Pb_{18}Se_{18}$	Face {100}	Cuboidal
$Pb_{18}Se_{18}$	Edge	Cuboidal
$Pb_{18}Se_{18}$	Vertex	Cuboidal
$Pb_{22}Se_{23}$	Face {100}	Cuboidal
$Pb_{22}Se_{23}$	Edge	Cuboidal
$Pb_{22}Se_{23}$	Vertex	Cuboidal
$Pb_{23}Se_{22}$	Face {100}	Cuboidal
$Pb_{23}Se_{22}$	Face {100}	Cuboidal
$Pb_{23}Se_{22}$	Edge	Cuboidal
$Pb_{23}Se_{22}$	Vertex	Cuboidal
$Pb_{24}Se_{24}$	Face {100}	Cuboidal
$Pb_{24}Se_{24}$	Face {100}	Cuboidal
$Pb_{24}Se_{24}$	Edge	Cuboidal
$Pb_{24}Se_{24}$	Edge	Cuboidal
$Pb_{24}Se_{24}$	Vertex	Cuboidal

Table 3.2: PbSe-Methylamine adducts: cluster stoichiometry, adsorption site and cluster morphology.

cases, two calculations were performed for the same cluster using two non-equivalent face or edge Pb atoms as adsorption sites. For methylamine, adducts with multiple ligand molecules ($Pb_xSe_xMA_y$, with x = 4, 6, 8, 9, 10 and $1 \leq y \leq x$) were generated in order to study the dependence of E_a on surface coverage. In these calculations, addition energies were corrected with Grimme's parametric method[39] to account for dispersion energy.

3.9 Quantum Dot Doping

It has recently been proposed that doping could prove to be a useful way to further tune the electronic and optical properties of quantum dots in general [69, 70, 71, 72] and in QDSSCs in particular [73]. Little work has been done to investigate doping in PbSe nanocrystals, especially of a computational nature: in order to gain a better understanding of the introduction of foreign elements in PbSe QDs, a series of calculations have been performed by replacing Pb atoms with tin, a common dopant in semiconductor quantum dots, germanium and barium, which all form cubic selenides (albeit at $T > 651$ °C in the case of Ge) and should therefore not disrupt the structure of PbSe. Clusters with formula $Pb_{32-x}Se_{32}D_x$ (D = Sn, Ge, Ba; x = 1, 2, 3, 4) were optimized.

3.10 Computational Details

Calculations on slabs were performed at DFT level with Crystal 09[74, 75] using periodic boundary conditions and localized gaussian-type basis sets (LANL2DZ[76, 77, 78] for Pb and Se and 6-31G(d,p)[79, 80] for all other atoms) within the Density Functional Theory framework at B3LYP[83] level. Geometry optimizations on finite clusters were also done at B3LYP level using the TURBOMOLE 6[84] software package, with localized gaussian-type

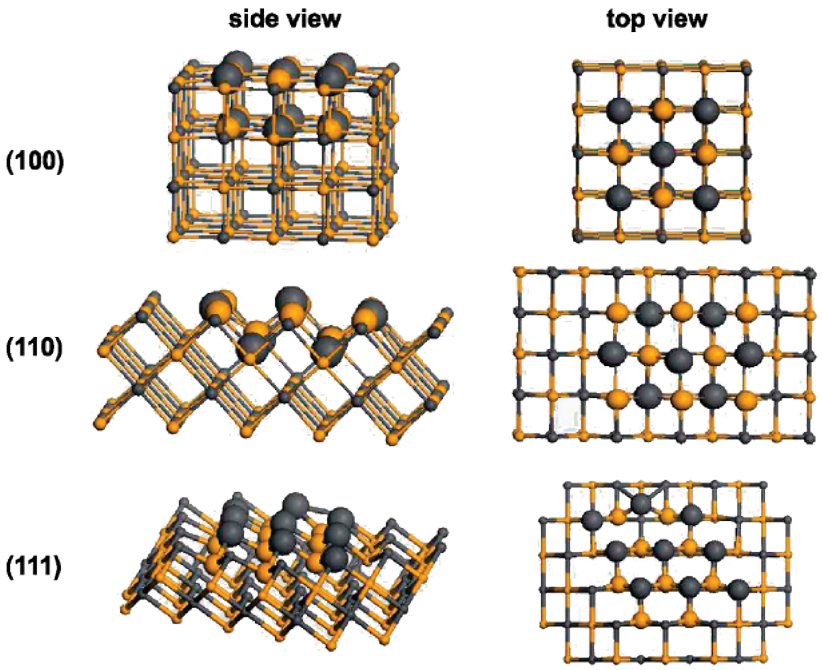

Figure 3.9: Three clusters of formula $Pb_{50}Se_{50}$. Large spheres indicate the atoms the positions of which were optimized, small spheres represent atoms that were kept in the initial position.

basis sets: 6-31G(d,p) for H, C, N, O and P atoms and LANL2DZ for all other elements, with added polarization functions[87] except for calculations described in Section 3.9. Isodensity surfaces were generated with Gaussian 09[85]. In the preliminary study of surfaces on the three $Pb_{50}Se_{50}$ clusters described in Section 3.2, only the positions of the first two atomic layers of the face of interest were optimized (Figure 3.9). In periodic calculations, both cell parameters and atomic positions were optimized, and 130 k points were included in the Brillouin zone.

Chapter 4

Results

> Thus do many calculations lead to victory, and few calculations to defeat.
>
> Sun Tzu
> The Art of War

4.1 Level of Theory

Comparison of the energy difference between the two semioccupied orbitals in the triplet state (ΔE_t) and the HOMO-LUMO gap in the singlet state (ΔE_s) (Figure 4.1) showed that the smallest $\Delta E_t - \Delta E_s$ difference was had when the BLYP functional was used, while the same quantity was significantly overestimated by B3LYP and even more so at HF level. This is consistent with electronic structure calculations performed on very similar system PbS by von Oertzen et al.[89], which predicted a band gap with an error below 0.1 eV with respect to the experimental value using a GGA functional, while B3LYP and HF gave errors of 1.6 and 5.7 eV, respectively. For

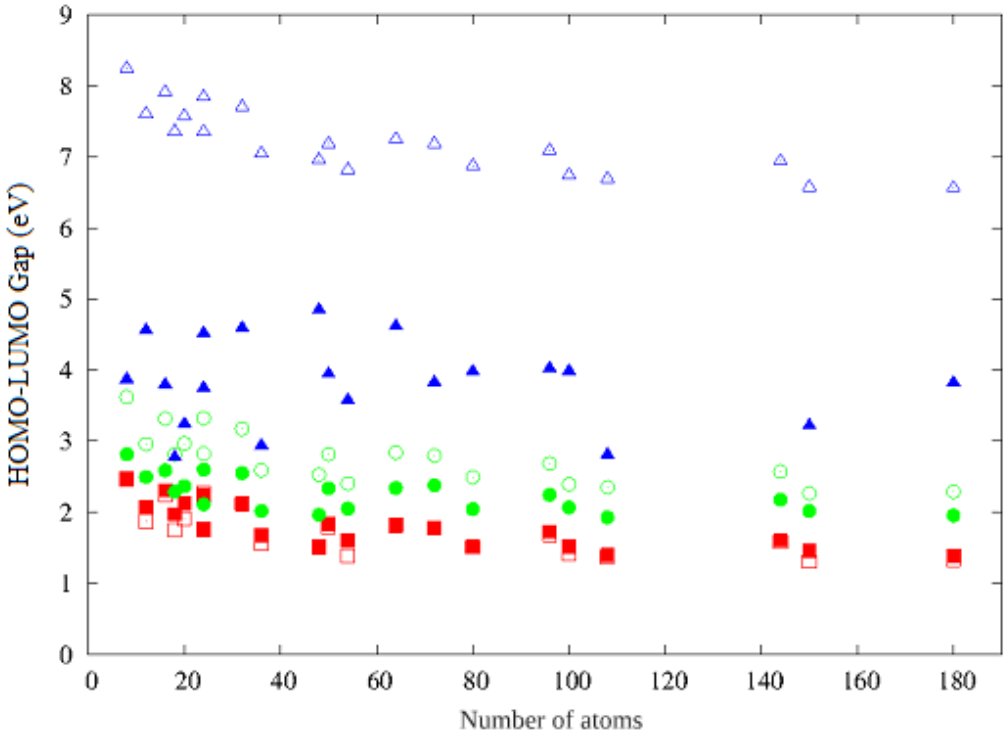

Figure 4.1: HOMO-LUMO gaps of cuboidal clusters of PbSe computed at BLYP (red squares), B3LYP (green circles) and Hartree-Fock (blue triangles) level in singlet (filled) and triplet (empty) states. For triplet state calculations, the gap is taken as the ΔE between the two semioccupied orbitals.

PbSe slab cell parameters

	a (Å)	b (Å)	γ (°)
{100}	4.4539	4.4539	90
{110}	4.4751	6.2719	90
{111}	4.4034	4.4034	120

Table 4.1: Cell parameters for PbSe slabs.

	Primitive Cell Area (Å^2)	E_c (eV)	E_s (eV)	$\overline{E}_s$ (eV Å$^{-2} \times 10^{-2}$)
{100}	19.84	1.306	0.686	1.73
{110}	28.07	2.630	1.789	3.19
{111} (Pb)	16.79	4.132	2.804	7.53
{111} (Se)				9.19

Table 4.2: Cell area, cleavage energy (E_c), surface energy (E_s) and normalized surface energy $\overline{E}_s$ of PbSe periodic slabs.

all calculations performed to investigate the electronic structure of clusters, the BLYP functional was therefore used.

4.2 Surface Stability and Ligands

4.2.1 Periodic Slabs

The optimized primitive cell of PbSe is defined by edges a = b = c = 4.4647 Å and angles $\alpha = \beta = \gamma = 60°$, with a corresponding lattice parameter a_0 = 6.3141 Å, which is approximately 0.2 Ågreater than the experimental value of 6.12 Å. Cleavage energy E_c and surface energy E_s were calculated for different slabs of increasing thickness, and it was found that slabs made of eight atomic layers had a sufficiently bulk-like internal region, so that both E_c and E_s remained essentially unchanged as the slab thickness was increased further.

	Ligand:Pb = 1:2			Ligand:Pb = 1:8		
	TMPO	MA	PA	TMPO	MA	PA
{100}	-0.52	-0.80	-0.75	-1.76	-0.87	-0.79
{110}	-1.24	-0.89	-0.97	-1.34	-0.91	-1.00
{111}	-0.26	-0.45	-0.21	-0.56	-0.49	-0.27

Table 4.3: Addition energies (eV) of TMPO, MA and PA on periodic PbSe slabs at different coverage.

Primitive cell stoichiometry was therefore Pb_8Se_8 for {100} and {110} slabs and Pb_4Se_4 for {111} slabs: this difference is due to the fact that, as described in section 3.2, {100} and {110} surfaces feature both Pb and Se atoms and, consequently, each atomic layer will have an equal number of Pb and Se atoms, while in {111} surfaces, only atoms of one type are present and, therefore, slabs of this type are composed of alternating Pb and Se layers. Cell parameters for each slab type are reported in Table 4.1, cleavage and surface energies in Table 4.2. Addition energies of MA, TMPO and PA are reported in table 4.3.

Results clearly indicate that the order of stability of the three surface types is {100} > {110} » {111}. Pb-terminated {111} surfaces are shown to be more stable than Se-terminated ones: this is in good agreement with experimental evidence[66]. The study of PbSe-ligand adducts has evidenced that E_a tends to decrease with increasing ligand coverage: this is likely the result of ligand-ligand interactions, which would explain the significant decrease of E_a observed for TMPO, the most sterically hindered of the three molecules. With a Ligand:Pb ratio of 1:8, TMPO adducts have the greatest E_a, with the strongest interaction occurring with the {100} slab. MA and PA exhibit a similar E_a value on {110} surfaces, while on {111} slabs the former is more than twice the latter. At higher coverage, {100} and {111} surfaces favour MA, while TMPO still gives the greatest E_a on {110} slabs, probably due to the greater distance between surface Pb atoms compared to the other two slabs. Based on these results, it is possible to estimate the effect of ligands on the relative stability of surfaces: it is immediately evident

that, for {111} surfaces, the interaction of MA, PA and TMPO is too weak to make any significant difference, while it could be proposed that the significantly greater E_a of TMPO on the {110} compared to the value for the {100} adduct could inverse the order of stability and favour the growth of {110} surfaces in nanocrystals: a Pb:ligand ratio of 2:1 requires a $2\times1\times1$ supercell, which would have a surface energy of $2A\overline{E}_s = 2\times28.07\times3.19\times10^{-2} = 1.79$ eV for {110} and $2\times19.84\times1.73\times10^{-2} = 0.69$ eV for {100}. The difference between the two E_a values is only 0.72 eV, while the surface energy of the {100} supercell is lower by 1.1 eV compared to the {110} supercell, therefore, the effect of TMPO on {110} surfaces is insufficient to invert the order of stability and favour the growth of this surface type.

4.2.2 Finite Clusters

Again, ligands appear to bind preferentially to Pb atoms (Figure 4.2): TMPO, MA and PA bind to a single Pb atom on {100} surfaces, while on {110} and {111} surfaces they tend to form adducts with a bridge geometry between two and three Pb atoms, respectively. PA^-, the only bidentate ligand used, binds to two Pb atoms on the {100} cluster, while in the other two adducts one oxygen atom is bound to one lead atom while the other oxygen atom is approximately equidistant from two Pb atoms. Addition energies for TMPO, MA, PA and PA^- are reported in Table 4.4.

Table 4.4: Counterpoise-corrected addition energies (eV) of a single TMPO, MA, PA and PA^- molecule/ion to $Pb_{50}Se_{50}$ clusters.

	TMPO	MA	PA	PA^-
{100}	-0.55	-0.47	-0.37	-3.13
{110}	-0.86	-0.57	-0.55	-3.83
{111}	-0.60	-0.25	-0.13	-4.42

Comparison of results on periodic slabs at low coverage and finite clusters reveals that in the latter case, addition energies tend to be smaller. The difference between the two sets of results can be explained as an effect of the

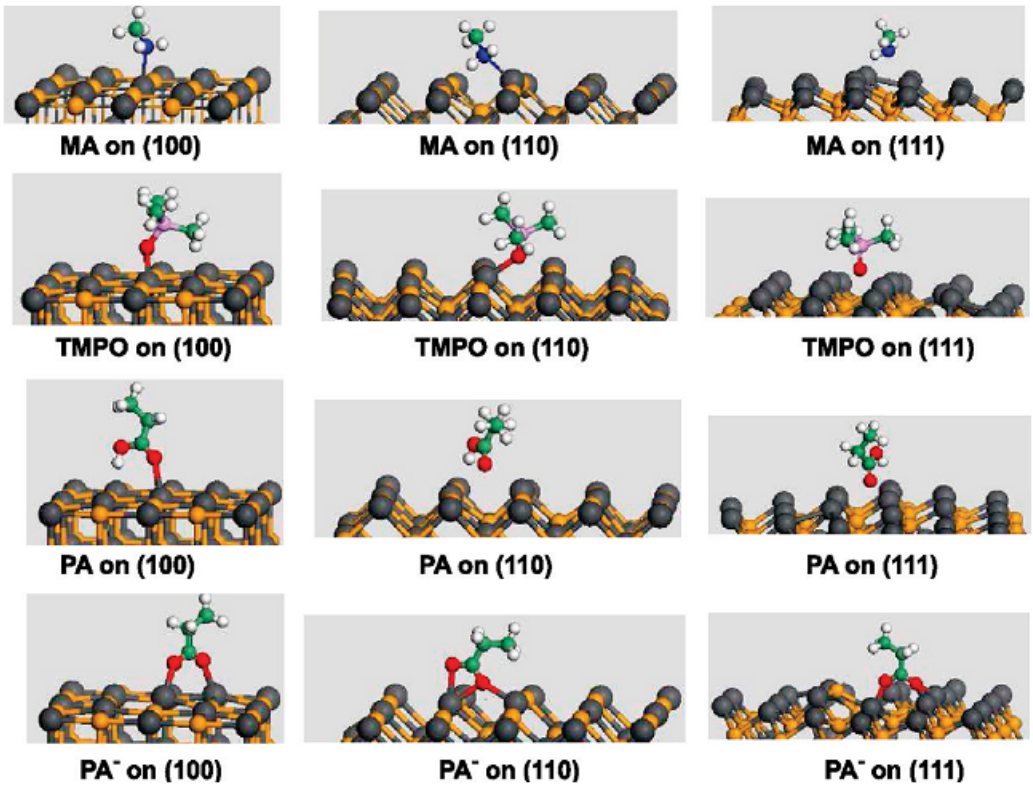

Figure 4.2: Ligand-$Pb_{50}Se_{50}$ adducts.

correction in finite cluster calculations of the basis set superposition error, which was in all cases below 0.50 eV. The only exception was the E_a value for the TMPO-{111} adduct, which was slightly greater in the finite cluster: this can be explained by noting that optimization of the systems produced slightly different geometries, with $Pb - \hat{O} - P \approx 90°$ in periodic slabs, while in the finite cluster, the oxygen atom is approximately equidistant from three Pb atoms. Similarly to what could be observed in the results from calculations on periodic slabs, TMPO tends to have a greater addition energy on all three surfaces than both MA and PA, however, the greatest addition energy is by far that of propanoate ion, the calculated E_a of which is one order of magnitude greater than the others in all adducts. In particular, it can be noted that E_a {111} > E_a{110} > E_a{100}. This result can be interpreted as a result of charge delocalization from the ligand on undercoordinated, electron-deficient lead atoms, which would also explain the affinity shown for Pb-rich {111} surfaces. For a surface type to be more stable than {100}, the following condition needs to be met:

$$n(A_x\overline{E}_{s,x} - A_{100}\overline{E}_{s,100}) \leq (E_{add,100} - E_{add,x}) \tag{4.1}$$

with x and n being the miller indices of the surface type and the number of surface primitive cells per ligand, respectively. The left hand side of the inequation represents the difference in stability of a surface with respect to the {100} surface, while the quantity on the right hand side is the difference in addition energy of a ligand on a surface compared to that of the ligand-{100} adduct. By applying the inequation, one can show that {111} > {100} when n > 1.4 and {110} > {100} when n > 1.3.

4.3 Cuboidal Clusters

Geometry optimization of cuboidal clusters has produced structures which retain the starting morphology, with minimal changes in bond angles and

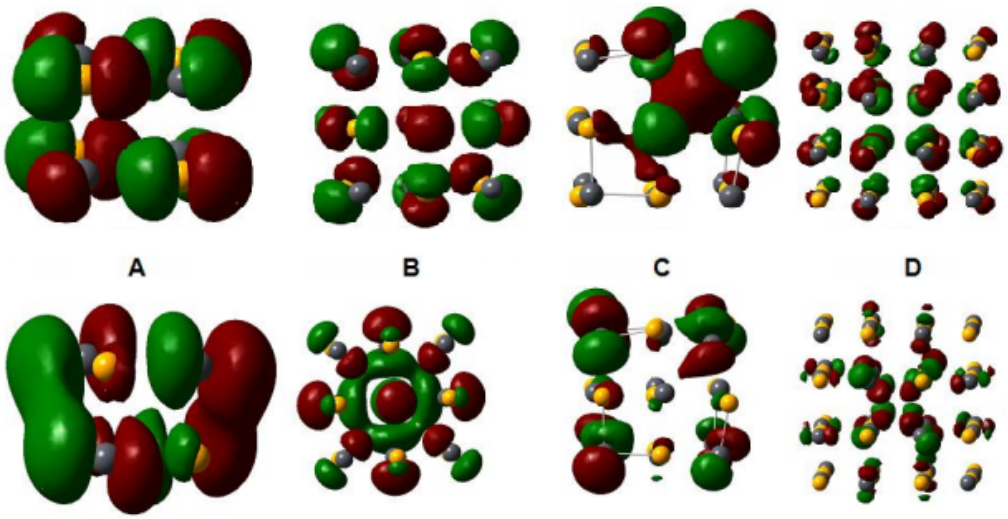

Figure 4.3: HOMO (top) and LUMO (bottom) (threshold = 0.02 $Å^{-3}$) of Pb_4Se_4 (A), Pb_9Se_9 (B), $Pb_{14}Se_{13}$ (C) and $Pb_{32}Se_{32}$ (D)

lengths. HOMO and LUMO are delocalized over the whole structure, with lobes centered on Se and Pb atoms, respectively (Figure 4.3).

4.4 Cuboctahedral and Octahedral Clusters

The optimized structures retained the starting morphology, with the relative positions of bulk atoms left almost unchanged, though moderate surface reconstruction occurred on {111} surfaces. Frontier orbitals appear noticeably less delocalized than in cuboids, with both HOMO and LUMO lobes centered on surface Pb atoms (Figure 4.4): this point will be further explored in Section 4.5.2.

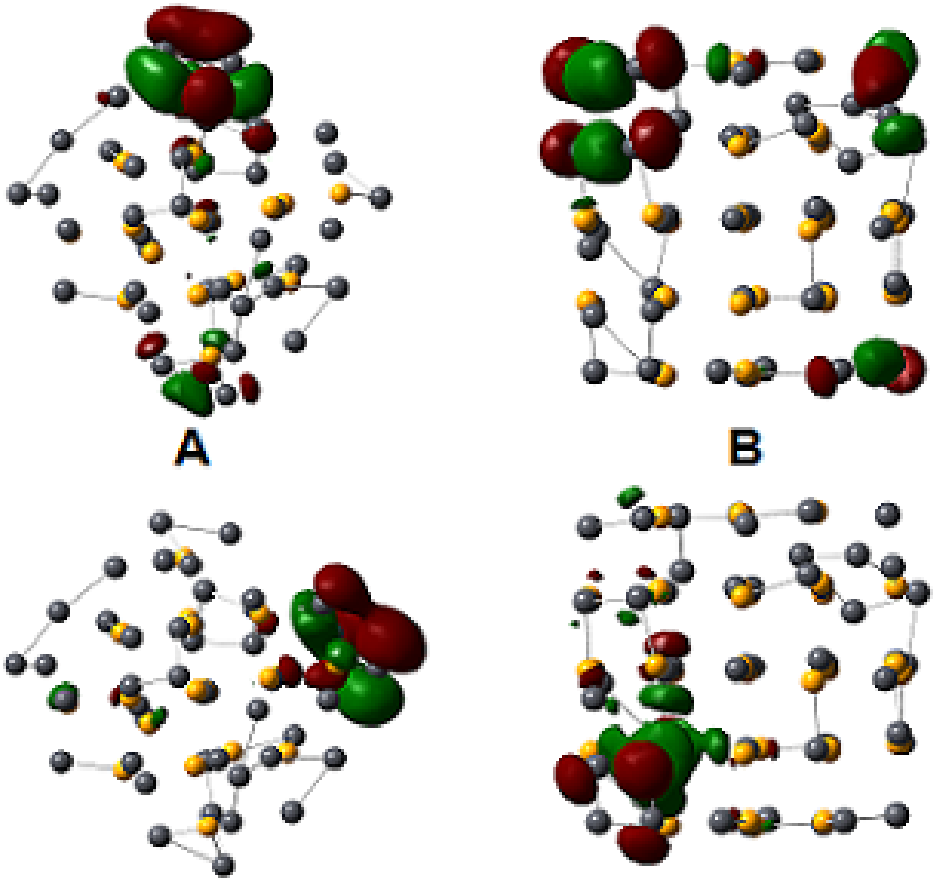

Figure 4.4: HOMO (top) and LUMO (bottom) of octahedral $Pb_{44}Se_{19}$ (A) and $Pb_{55}Se_{38}$ (B).

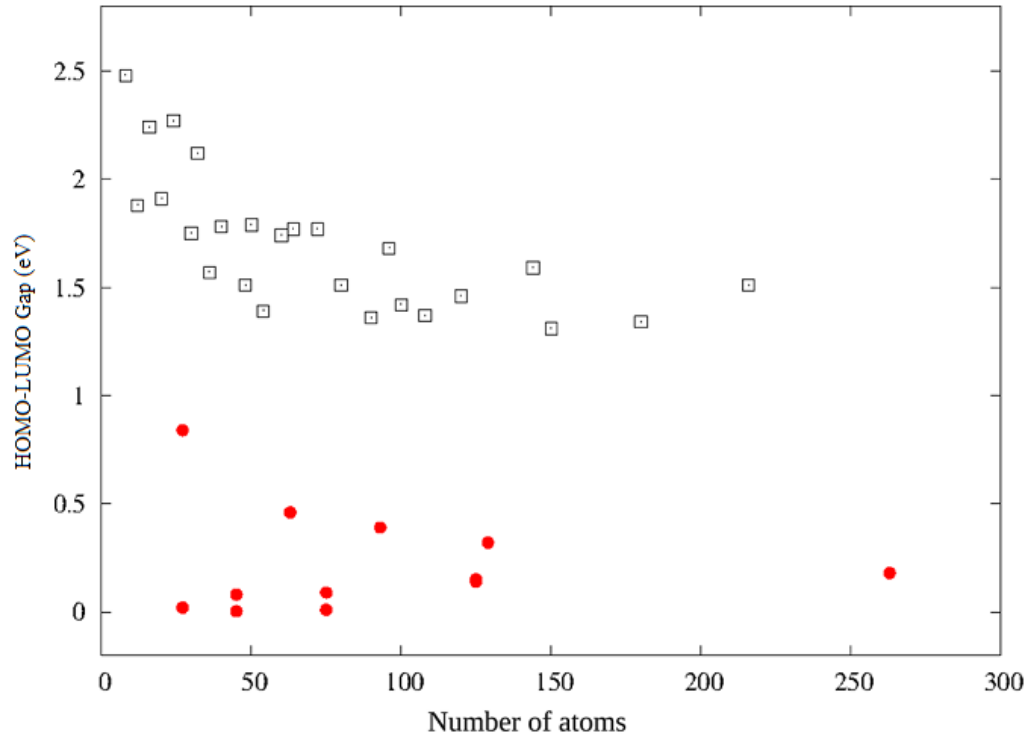

Figure 4.5: HOMO-LUMO gaps of PbSe nanocrystals as a function of the number of cluster atoms. Black squares: stoichiometric clusters; red circles: non-stoichiometric clusters.

4.5 Electronic Structure

4.5.1 HOMO-LUMO Gaps

The calculated HOMO-LUMO gaps of PbSe clusters are reported in Figure 4.5. By plotting the HOMO-LUMO gaps E_g as a function of nanocrystal atom number, the presence of two distinct families emerges: stoichiometric and non-stoichiometric, with the former having a greater gap. E_g values for stoichiometric clusters fall in the 1.25-2.5 eV region and tend to decrease as the number of atoms increases: this behaviour is consistent with the well known quantum size effect. The decrease in E_g with increasing cluster size is less evident in non-stoichiometric clusters, for reasons that will be explained

in section 4.5.2.

4.5.2 Effect of Stoichiometry

Examination of the densities of states of nanocrystals revealed that stoichiometric clusters present a "clean" band gap (Figure 4.6), while non-stoichiometric clusters are characterized by the presence of intra-gap states (IGSs) (Figure 4.7). This appears to be true independetly of nanocrystal morphology: clusters with a Pb : Se $\neq$ 1 ratio of cuboidal, cuboctahedral and octahedral shape all exhibit IGSs. In clusters with an excess of lead atoms, the IGSs are occupied orbitals, whereas clusters with a Pb:Se $<$ 1 ratio present virtual IGSs (Figure 4.7). Virtual IGSs appear much closer to the valence band compared to occupied IGSs: this may explain the lack of a clear trend in E_g vs. atom number in non-stoichiometric nanocrystals in Figure 4.5. For comparative purposes, calculations were also performed on two non-cubic clusters with formula $Pb_{59}Se_{56}$ and $Pb_{56}Se_{59}$: as expected, three IGSs were observed in both the Pb-rich and the Se-rich clusters, which were occupied in the former and virtual in the latter. As in the cubic crystals, the IGSs in the Se-rich cluster were closer to the valence band than those in the Pb-rich cluster (Figure 4.8.

Upon closer inspection, it was noted that the number of intra gap states is strictly a function of cluster stoichiometry (Figure 4.9), with the number of IGSs (N_{IGS}) always equal to stoichiometric excess:

$$N_{IGS} = |N_{Pb} - N_{Se}| \tag{4.2}$$

this relation was verified for all clusters studied 4.9. Given this definition of intra gap states, it is possible to recalculate the HOMO-LUMO gap without considering IGSs (Figure 4.10).

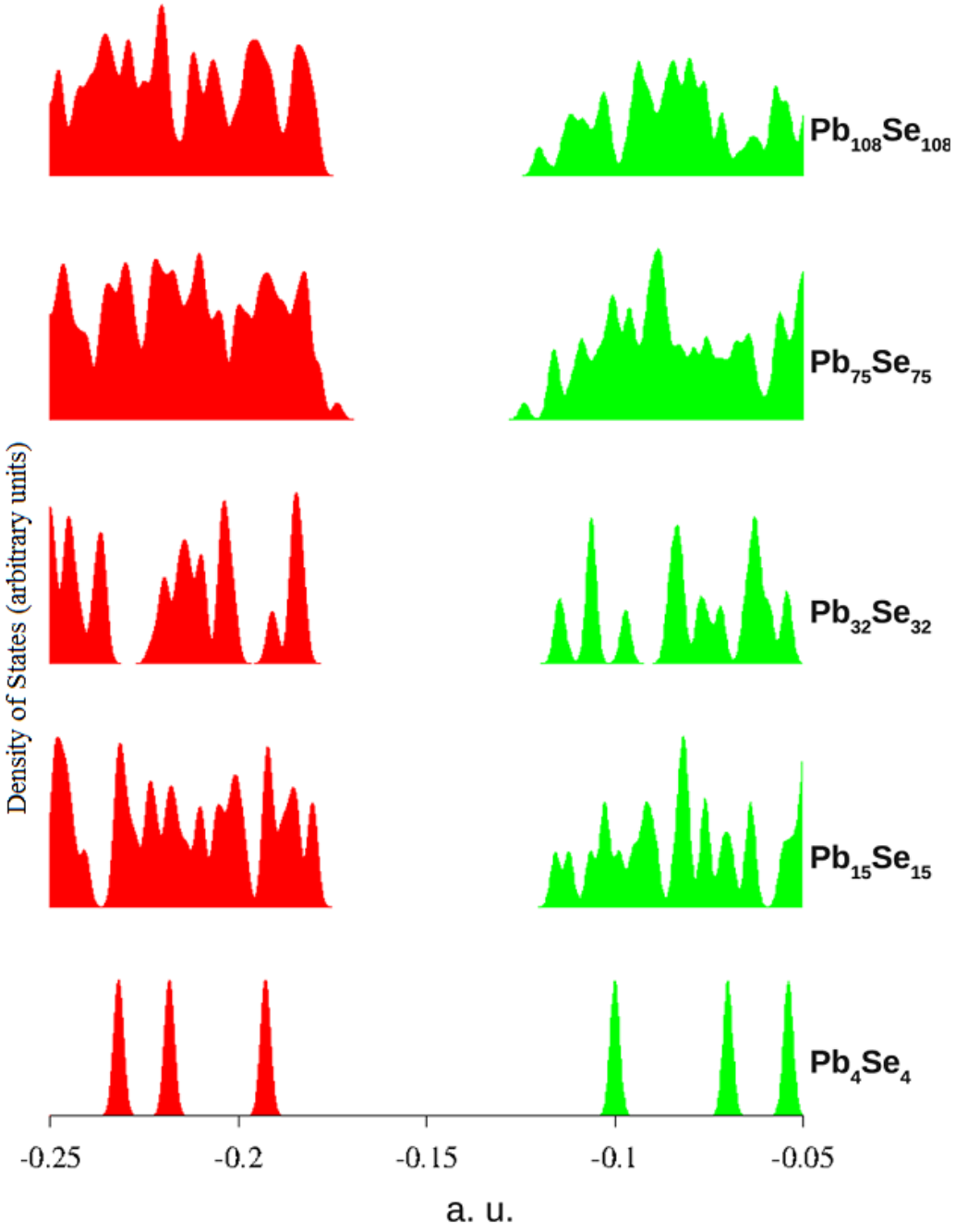

Figure 4.6: Densities of states of five stoichiometric cuboidal PbSe nanocrystals. States are represented as red (occupied) and green (virtual) gaussian functions of unitary height (arbitrary units) and 0.003 eV width.

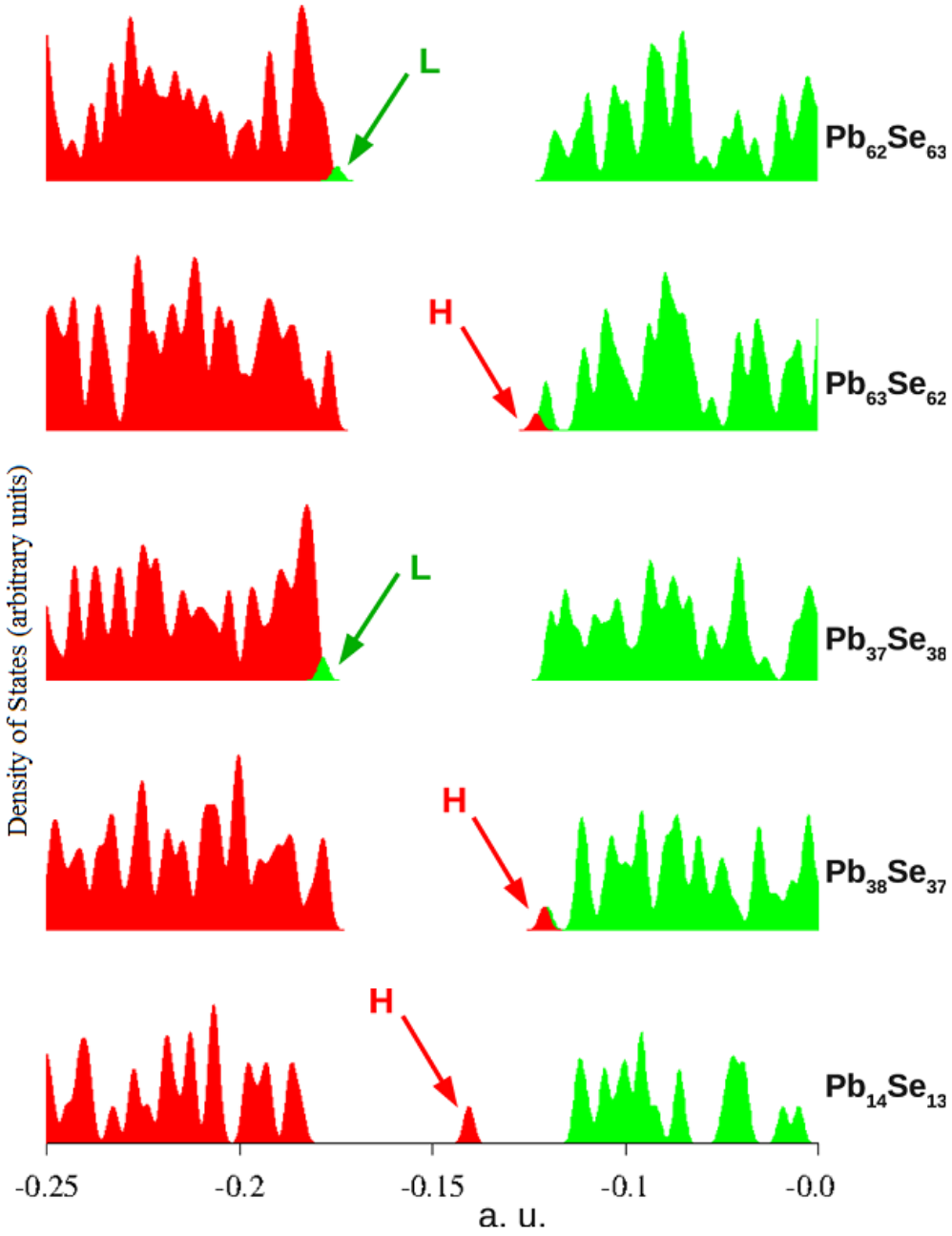

Figure 4.7: Densities of states of five non-stoichiometric cuboidal PbSe nanocrystals. States are represented as red (occupied) and green (virtual) gaussian functions of unitary height (arbitrary units) and 0.003 eV width. Arrows indicate HOMO (H) and LUMO (L).

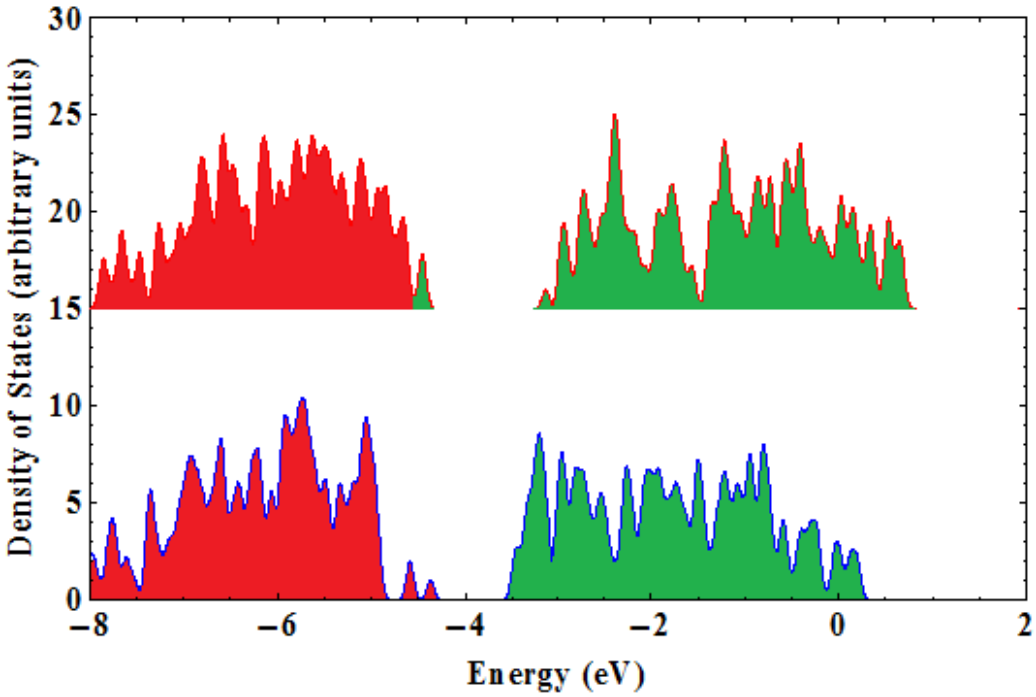

Figure 4.8: Densities of states of $Pb_{59}Se_{56}$ and $Pb_{56}Se_{59}$. States are represented as red (occupied) and green (virtual) gaussian functions of unitary height (arbitrary units) and 0.003 eV width. Arrows indicate HOMO (H) and LUMO (L).

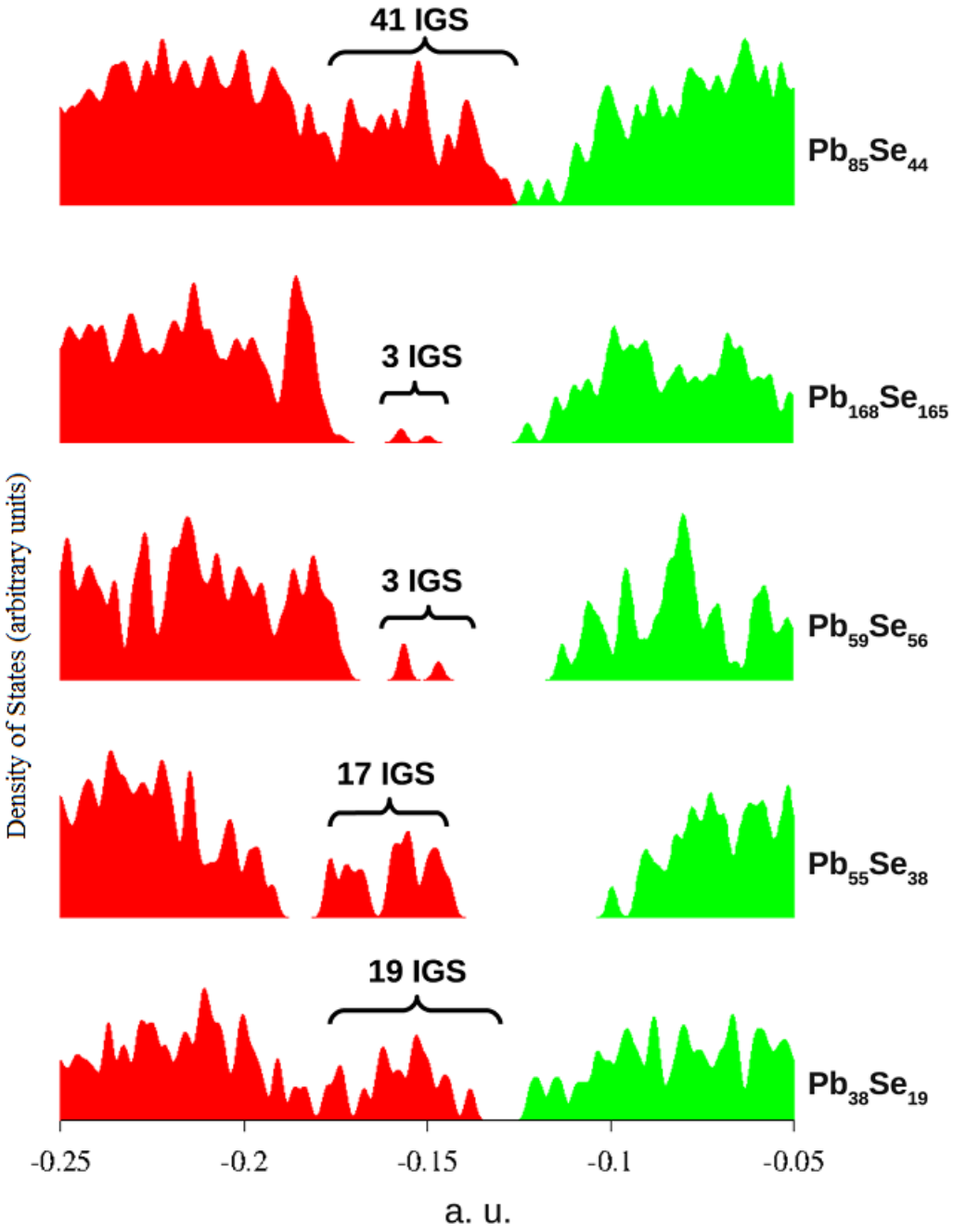

Figure 4.9: Densities of states of five cuboctahedral and octahedral PbSe nanocrystals. States are represented as red (occupied) and green (virtual) gaussian functions of unitary height (arbitrary units) and 0.003 eV width. Intra gap states are evidenced.

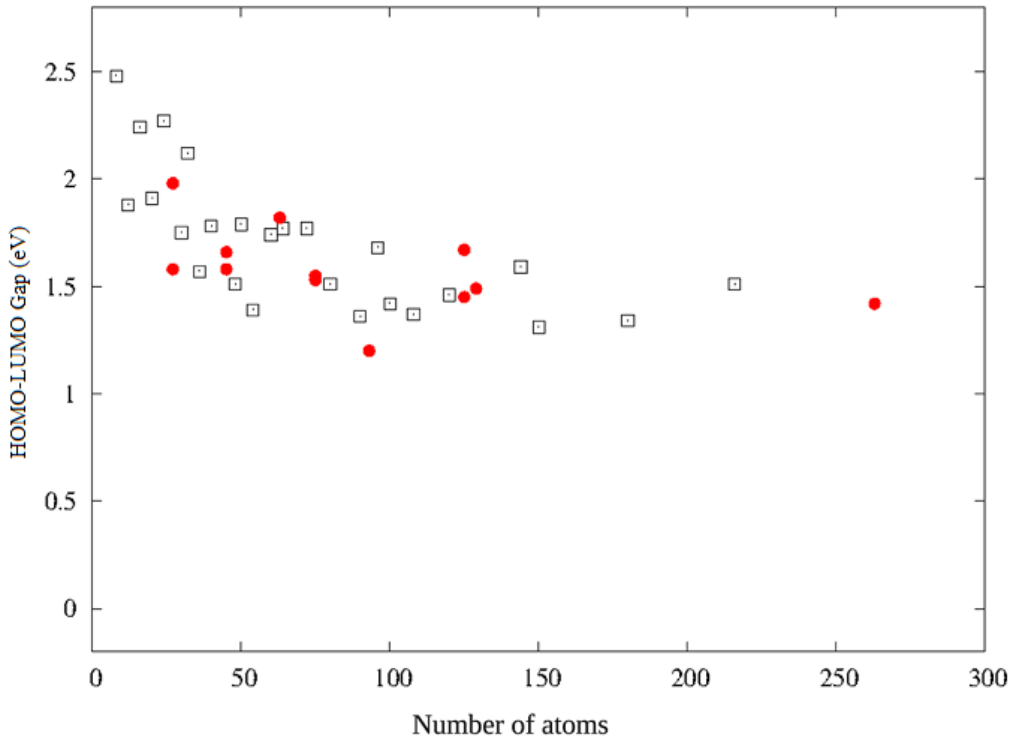

Figure 4.10: HOMO-LUMO gaps of PbSe nanocrystals (excluding IGSs) as a function of the number of cluster atoms. Black squares: stoichiometric clusters; red circles: non-stoichiometric clusters.

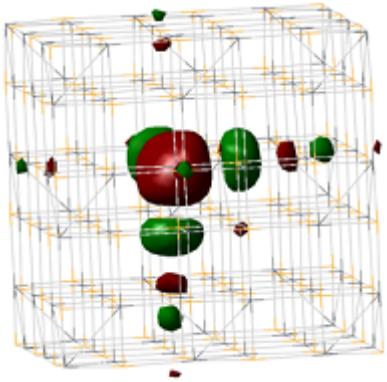

Figure 4.11: Isodensity surface (threshold 0.02 Å^3) for the IGS in $Pb_{107}Se_{108}$.

4.5.3 Effect of Morphology

As described in Section 3.6, cluster stoichiometry and morphology are strictly related, with cuboctahedra and octahedra being intrinsically non-stoichiometric. In order to elucidate the influence of morphology on PbSe nanocrystal electronic structure independently from stoichiometry, a stoichiometric cluster with formula $Pb_{28}Se_{28}$ exposing {111} faces and a non-stoichiometric cubic cluster with formula $Pb_{108}Se_{107}$, obtained by removing a bulk Se atom from the stoichiometric cube, were studied. Again, the stoichiometric cluster had no intra gap states and an E_g of 1.14 eV, while the non-stoichiometric one had a single occupied IGS, consistently with calculations on other nanocrystals, which was delocalized around the vacancy (Figure 4.11).

4.5.4 Effect of Ligands

The effects of surface passivation on electronic structure were studied by comparing the density of states of the bare $Pb_{59}Se_{56}$ cluster with that of its adducts with model ligands. The energy eigenvalues of LUMO, IGSs and HOMO (or, more accurately, the top of the valence band) are reported in Table 4.5. The bare nanocrystal had three occupied IGSs, which were all

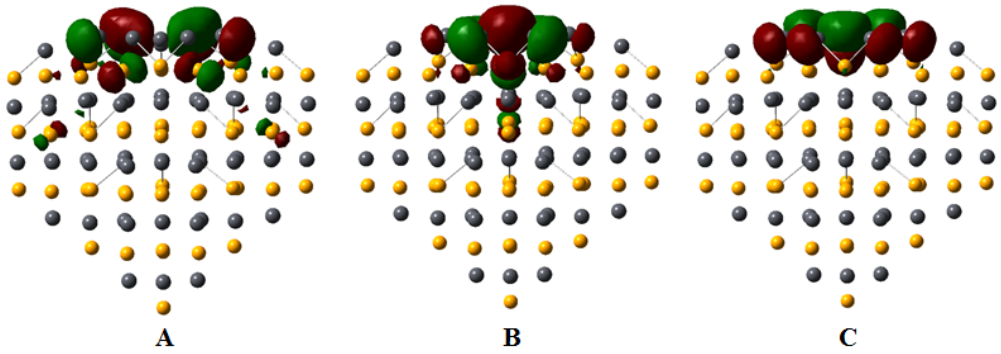

Figure 4.12: Isodensity surfaces of the three intra-gap states of $Pb_{59}Se_{56}$ (threshold = 0.02 $Å^{-3}$). A, B and C indicate the lowest, middle and highest energy IGS, respectively.

localized on the section of {111} surface (Figure 4.12), with the two lowest energy-IGSs being almost isoenergetic at -4.257 eV and the other one at 3.999 eV. Electrophilic ligands $Al(CH_3)_3$ and BCl_3 appear to have no significant influence on the electronic structure of the cluster and nucleophilic ligands (methylamine, phosphine, methanethiol and formic acid) only cause the energy eigenvalue of the HOMO to be slightly higher (< 0.1 eV) than in the bare cluster. Adsorption of one molecule of carbon monoxide results in the lowest lying IGS to shift closer to the top of the valence band by 0.293 eV, but is still distinctly an IGS, lying at 0.158 eV above the HOMO. Adducts with one sulphur atom, two ethyl radicals or two formiate ions show the most significant changes in electronic structure compared to the bare cluster, with the first IGS now energetically very close ($\Delta E < 0.1$ eV) to the HOMO. Based on these results, a further set of calculations was performed: adducts with two and three S atoms, and up to six CH_3CH_2 and $HCOO^-$, were generated. When two S atoms were adsorbed on the cluster, only one IGS was observed, while with three adsorbed S atoms no IGSs were left. Similar results were obtained with ethyl and formiate: with four adsorbed ligands, only one IGS was left, while adsorption of six ligands completely removed IGSs. Further confirmation that the IGSs are removed by these ligands can be derived by plotting the isodensity surfaces of the three highest occupied molecular orbitals in the $Pb_{59}Se_{56}(HCOO^-)_6$ adduct: while in the absence

Table 4.5: Energy eigenvalues (eV) of frontier orbitals of Pb59Se56 and its adducts with several model ligands. For $CH_3CH2^{\cdot}$ and $HCOO^-$, two ligands were used in each adduct.

Ligand	HOMO	IGS 1	IGS 2	IGS 3	LUMO
None	-4.701	-4.257	-4.257	-3.999	-3.081
$Al(CH_3)_3$	-4.703	-4.263	-4.249	-4.013	-3.084
BCl_3	-4.700	-4.256	-4.255	-4.001	-3.080
CO	-4.708	-4.550	-4.301	-3.842	-3.154
CH_3CH_2	-4.714	-4.680	-4.224	-3.767	-3.100
$HCOO^-$	-4.724	-4.668	-4.637	-3.993	-3.045
HCOOH	-4.613	-4.292	-4.280	-3.801	-3.005
CH_3NH_2	-4.626	-4.403	-4.400	-3.815	-3.032
PH_3	-4.658	-4.381	-4.379	-3.854	-3.056
S	-4.769	-4.709	-4.358	-4.031	-3.127
CH_3SH	-4.656	-4.360	-4.344	-3.855	-3.053

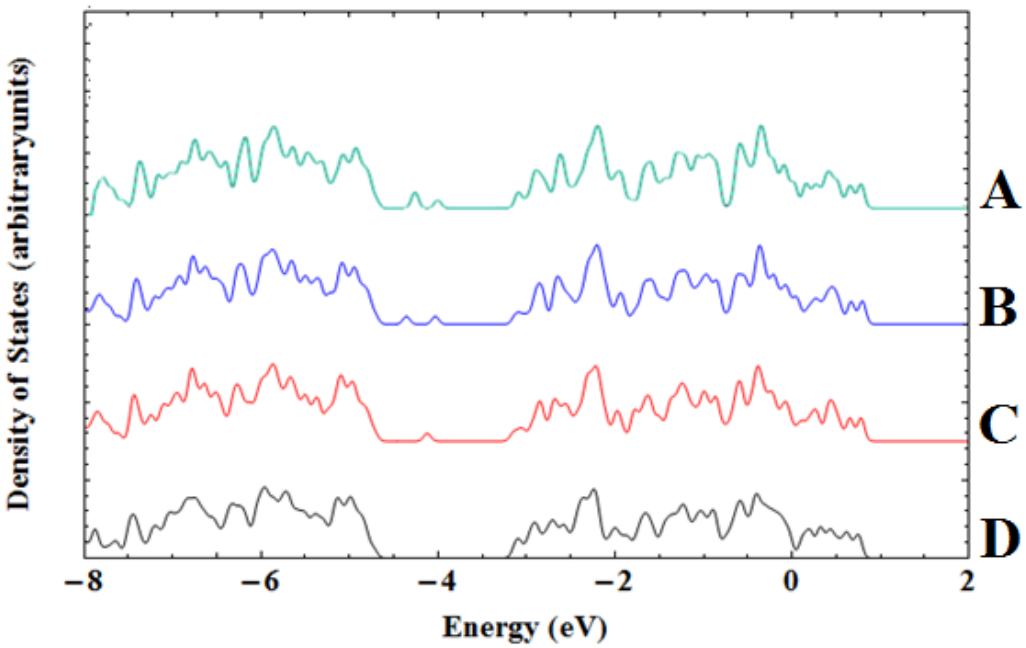

Figure 4.13: Density of states of $Pb_{59}Se_{56}$ bare (A), one S atom (B), two S atoms (C) and three S atoms (D). The graphs are obtained as a sum of gaussians centred on each state's corresponding energy eigenvalue, with unitary height and 0.003 eV width.

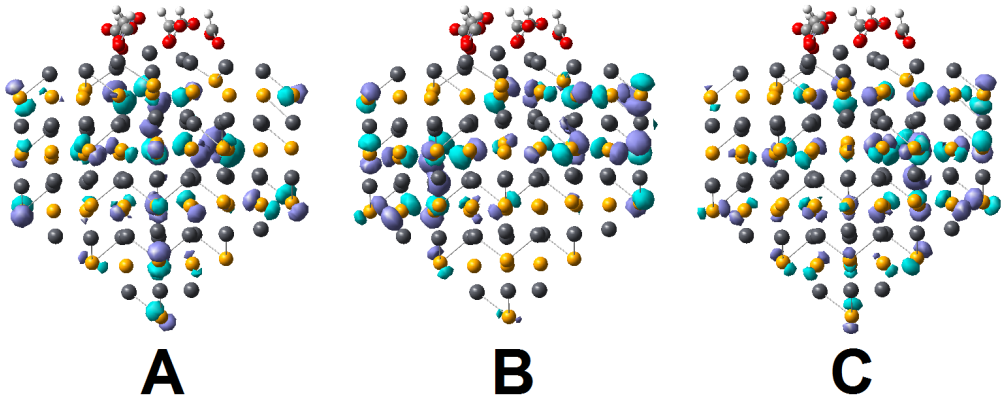

Figure 4.14: Isodensity surfaces of the three highest occupied molecular orbitals (A: third highest; B: second highest; C: highest) of $Pb_{59}Se_{56}(HCOO^{-})_6$.

of ligands these were noticeably localized on the {111} surface of the cluster, in the adduct they appear delocalized over the whole cluster (Fig. 4.14).

Though a systematic study of the effects of charge on electronic structure was beyond the scope of this work, three calculations were performed on the bare $Pb_{59}Se_{56}$ by setting the cluster charge to +2, +4 and +6: with a +2 charge, the cluster featured two occupied and one virtual IGS; when the charge was set to +4, only one occupied IGS was observed while two virtual IGSs were present; lastly, with a +6 charge, only three virtual IGSs were left. Calculations on negatively charged adducts $[Pb_{59}Se_{56}(HCOO^{-})_2]^{2-}$, $[Pb_{59}Se_{56}(HCOO^{-})_4]^{4-}$ and $[Pb_{59}Se_{56}(HCOO^{-})_6]^{6-}$ also showed no removal of IGSs. These results suggest that the effect of ligands on IGSs is due of an orbital energy shift, bur rather to the oxidation of excess lead atoms. Another result that points towards this conclusion is the removal of IGSs by ligands adsorbed on {100} surfaces (as opposed to {111}) on $Pb_{59}Se_{56}$, as well as in non-stoichiometric cubes. Adsorption of S, $HCOO^{-}$ and $CH_3CH_2^{\cdot}$ on systems with a clean band gap (such as stoichiometric cube $Pb_{32}Se_{32}$ and $Pb_{59}Se_{56}(HCOO^{-})_6$) produced new virtual intra-gap states.

4.6 Ligand Addition Energy

4.6.1 Different Adsorption Sites

Counterpoise-corrected addition energies of methylamine on surface Pb atoms located on {100} faces, edges and vertices of clusters were calculated (Figure 4.15). No clear pattern emerges, though a tenuous tendency of methylamine to give slightly greater addition energies on faces and edges than on vertices can be observed by comparing the average E_as (0.993, 0.844 and 0.729 eV for adducts on faces, edges and vertices, respectively). This result can be explained by noting that in vertex adducts, methylamine is farther away from other surface atoms than in edge and face adducts, where dispersion effects are therefore greater. Values for {100} adducts appear significantly greater than those reported in Section 4.2: this difference is ascribable to the inclusion of dispersion corrections. In all calculations, the basis set superposition error was in the order of 10^{-1} eV, consistently with results described in Section 4.2.2.

4.6.2 Number of Adsorbed Molecules

Adsorption of multiple methylamine molecules has shown that the average addition energy $\bar{E}_a$ decreases as the number of adsorbed ligands increases. This finding is consistent with results from periodic calculations described in Section 4.2. As methylamine is used as a model ligand to simulate the considerably larger hexadecylamine commonly used during post-synthetic procedures, it is likely that steric hindrance will further contribute to this effect.

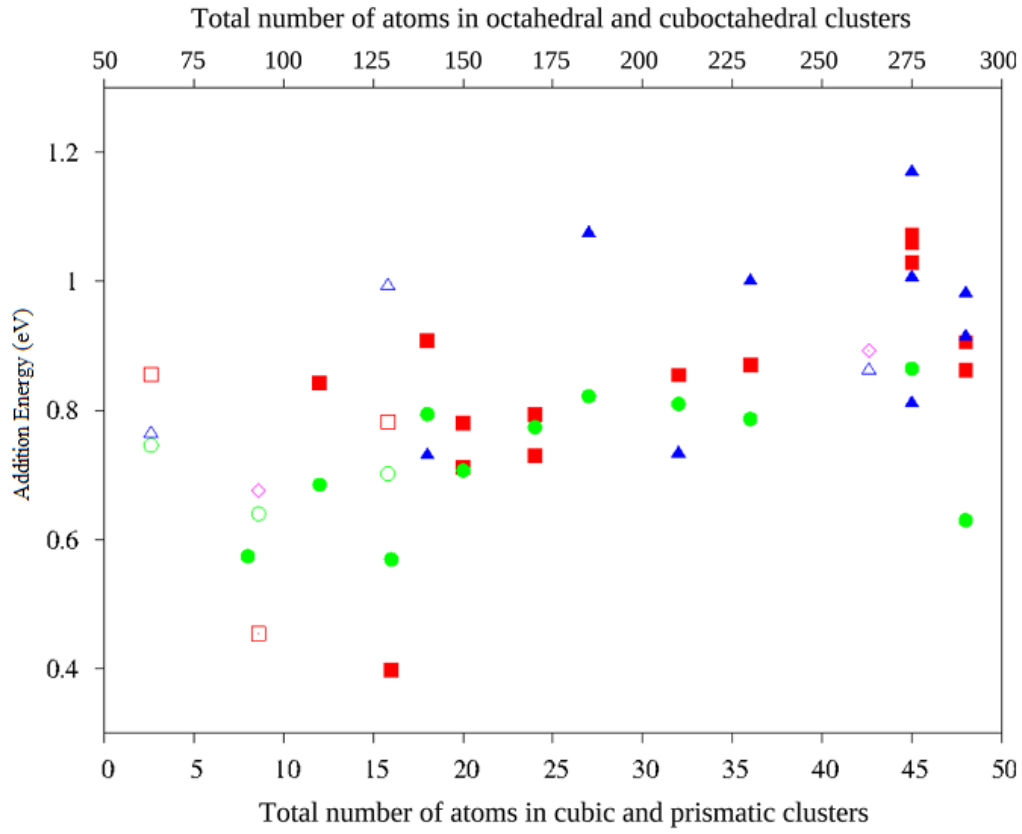

Figure 4.15: Counterpoise corrected-addition energy (eV) of methylamine on Pb atoms in different positions. Blue triangles: {100} face; pink rhombi: {111} face, red squares: edge; green circles: vertex; filled symbols: cuboidal clusters, empty symbols cuboctahedral or octahedral clusters.

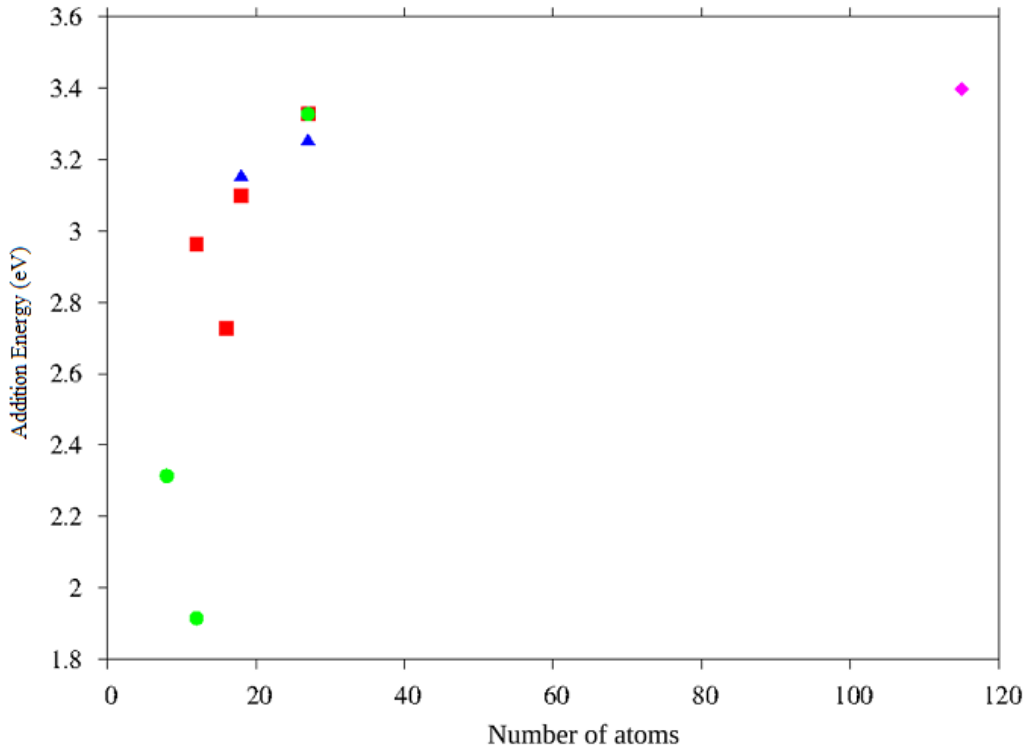

Figure 4.16: Counterpoise corrected-addition energy (eV) of formiate on Pb atoms in different positions. Blue triangles: {100} face; pink rhombi: {111} face, red squares: edge; green circles: vertex; filled symbols: cuboidal clusters, empty symbols cuboctahedral or octahedral clusters.

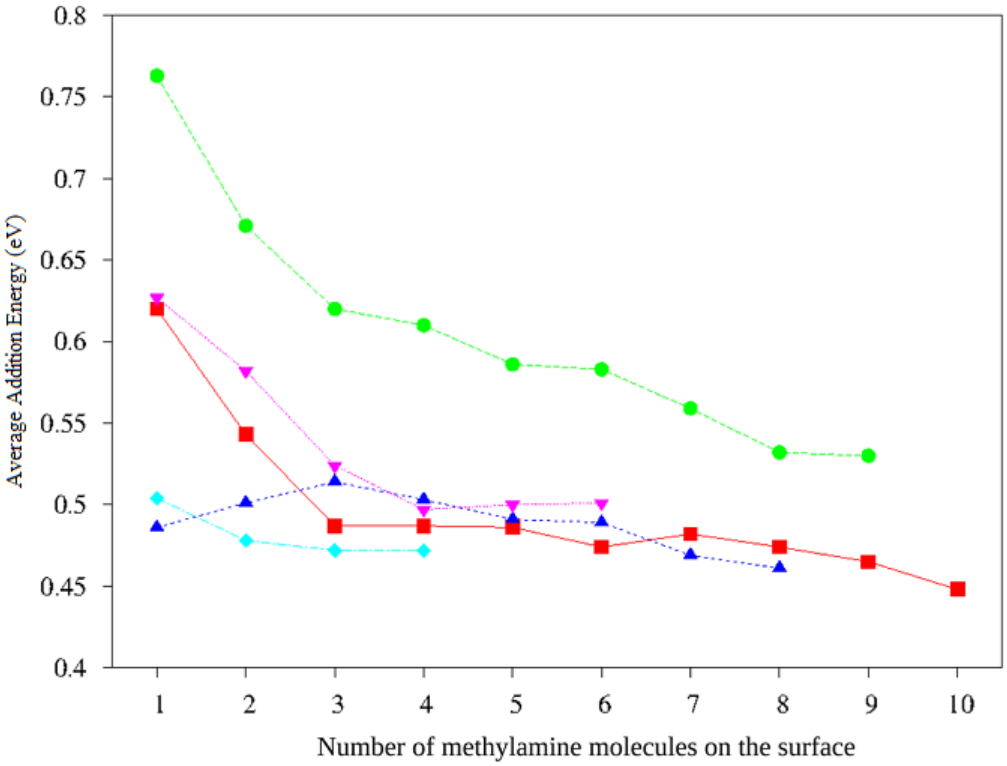

Figure 4.17: Counterpoise-corrected average addition energy of methylamine as a function of number of molecules adsorbed on different clusters. Cyan rhombi: Pb_4Se_4; pink down triangles: Pb_6Se_6; blue up triangles: Pb_8Se_8; green circles: Pb_9Se_9, red squares: Pb_10Se_10.

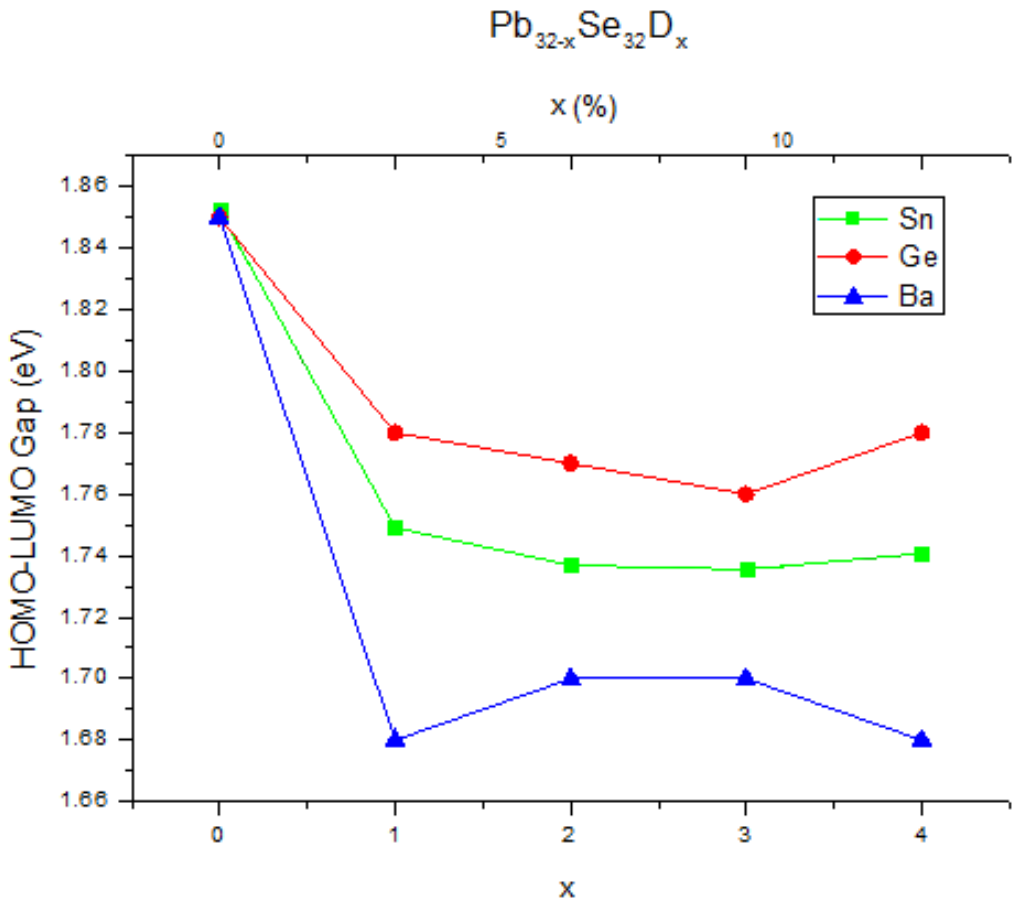

Figure 4.18: HOMO-LUMO gaps (eV) of clusters $Pb_{32-x}Se_{32}D_x$ as a function of x (D = Sn, Ge, Ba; x = 0, 1, 2, 3, 4).

4.7 Doping

The HOMO-LUMO gaps of the clusters obtained by replacing Pb atoms with Sn and Ge in $Pb_{32}Se_{32}$ are shown in Figure 4.18. A gerenal tendency of the HOMO-LUMO gap to decrease as the amount of dopant increases can be noticed, though in the case of x = 4 a small increase is observed for D = (Sn, Ge). The presence of dopant atoms also influences the energy levels of frontier orbitals: the HOMO energy E_{HOMO}, which in the pure PbSe cluster is -4.979 eV, is most visibly affected by Ba atoms, as E_{HOMO} was found to

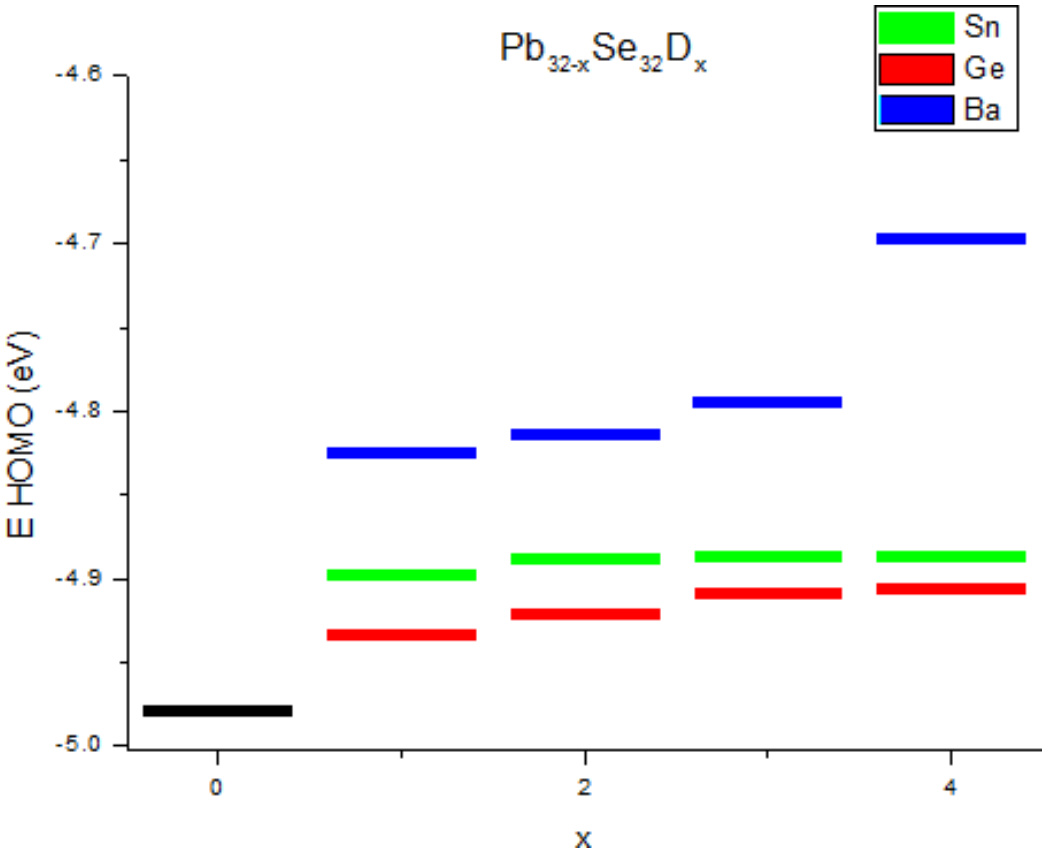

Figure 4.19: HOMO energy levels of $Pb_{32-x}Se_{32}D_x$ (D = Sn, Ge, Ba; $0 \leq$ x ≤ 5).

be -4.822 for x = 1, while the same amount of Sn and Ge caused E_{HOMO} to rise to -4.897 and -4.934 eV, respectively. Greater concentrations of D produced progressively smaller changes in E_{HOMO} for D = (Sn, Ge), while for D = Ba the change increased (Figure 4.19). Variations in E_{LUMO} were less pronounced, with one atom of Sn, Ge and Ba causing a drop from -3.127 eV to -3.148, -3.154 and -3.139 eV, respecively. Further substitutions of Pb atoms with dopants caused no significant changes for Sn, while Ge and Ba appear to increase E_{LUMO} (Figure 4.20).

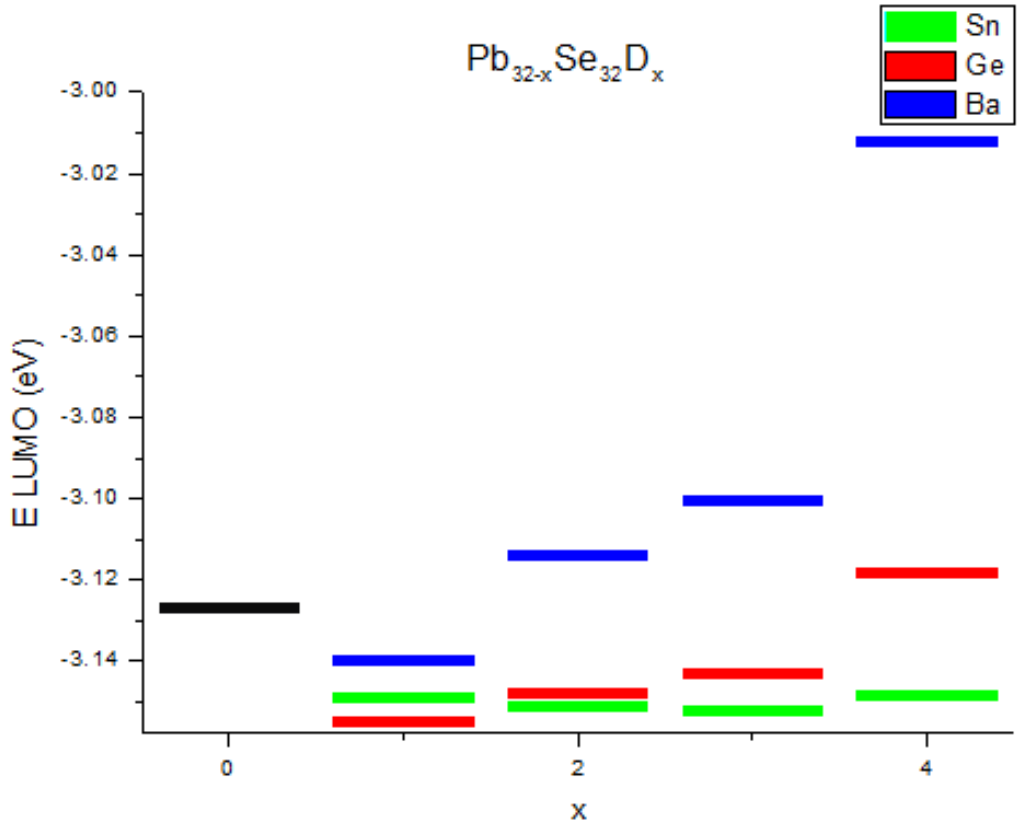

Figure 4.20: LUMO energy levels of $Pb_{32-x}Se_{32}D_x$ (D = Sn, Ge, Ba; 0 $\leq$ x $\leq$ 5).

Chapter 5

Conclusions

> Science is made up of so many things that appear obvious after they are explained.
>
> Frank Herbert
> Dune

5.1 PbSe Quantum Dot Growth and Morphology

From the results on both periodic and finite systems described in Section 4.2, it appears evident that Pb-{111}-carboxylate adducts are significantly more stable than all other adducts. This consideration has prompted the proposition of a growth model for colloidal PbSe QDs synthesized via the hot injection route: after nucleation, QDs likely appear multifaceted, exposing several types of surfaces. As the QDs grow in the presence of carboxylate ions, these will become adsorbed onto their surfaces,

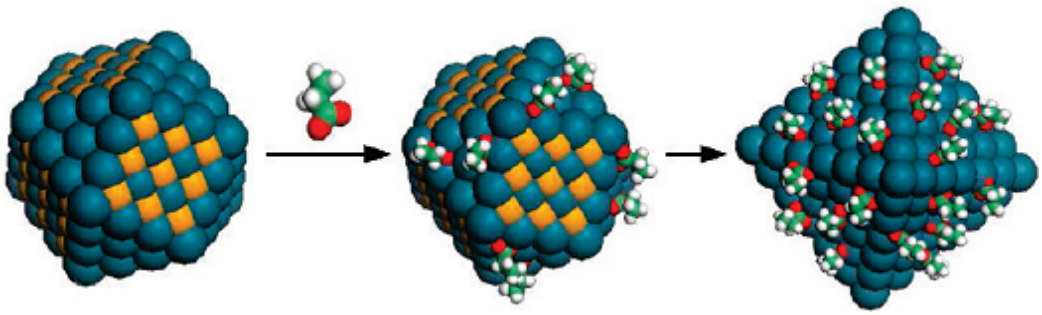

Figure 5.1: Proposed growth mechanism for colloidal PbSe quantum dots, from left to right: multifaceted cluster after nucleation; selective surface stabilization by carboxylates; final octahedral morphology.

forming different types of adducts. Pb-terminated {111} facets will keep growing due to the stabilizing effect provided by the adsorbed ligand, while other facets will undergo surface reconstruction, thus leading to a final QD morphology in which {111}-type facets are prevalent (Figure 5.1). Though a complete description of the growth and morphology of colloidal QDs should obviously include such factors as solvent, temperature, ligand and precursor concentration and ratio, this simple model predicts the existence of octahedral QDs, which have been experimentally observed [90, 91, 92]. The greater stability of {100} surfaces in the absence of ligands would also suggest that PbSe QDs synthesized through ligand-free routes should expose {100} facets, as is the case in cubes: this hypothesis finds confirmation in the experimental observation of PbSe nanocubes obtained via mechanochemical synthesis [93].

5.2 Stoichiometry, Morphology and Electronic Structure

Analysis of the densities of states of cuboidal, cuboctahedral and octahedral clusters have shown significant diversities, particularly, all uncapped octahedral and cuboctahedral clusters have IGSs, while most cuboidals do not. This effect has been shown to result from different nanocrystal stoi-

chiometry, rather than morphology, as the appearance of IGSs was verified in non-stoichiometric nanocrystals only, with $N_{IGS} = |N_{Pb} - N_{Se}|$. This was particularly evident in the two cubes of formula $Pb_{108}Se_{108}$ and $Pb_{107}Se_{108}$, the latter of which had been obtained by reoptimizing the structure after removal of a core Pb atom, while a stoichiometric cluster, $Pb_{28}Se_{28}$, exposing {111} surfaces, had a clean band gap.

5.3 Ligands and Electronic Structure

Results from calculations on adducts of PbSe clusters with ligands clearly point towards a strong dependence on the ligand type of the impact of capping agents on the electronic structure of PbSe nanocrystals. Carboxylates effectively remove IGSs, but a number of adsorbed carboxylates greater than the stoichiometric excess in the cluster induces the appearance of IGSs. The calculations performed on charged clusters and adducts suggest that the carboxylate-induced removal of IGSs is the result of the oxidation of the excess lead atoms rather than to an orbital energy shift. IGSs can also be removed by ligands capable of forming covalent bonds with the surface Pb atoms, as in the case of ethyl radicals and sulphur atoms. These results clearly indicate that ligands play a vital role in the definition of the electronic structure and, therefore, of the overall properties of PbSe quantum dots. Neither electrophilic nor common neutral ligands were effective at removing intra-gap states, though they still bind to the surface of PbSe. These results prove that ligand choice and control of surface chemistry are of capital importance for synthesizing PbSe quantum dots with the desired properties.

5.4 Doping

Substitution of Pb atoms with Sn, Ge and Ba reduces the HOMO-LUMO gap, more markedly so in the case of Ba than Sn and least of all for Ge. The energy level of the HOMO increases with increasing dopant concentration, while that of LUMO is less affected and appears to shift differently depending on dopant type and concentration. These calculations indicate that doping could prove to be a viable route to more accurately tune the properties of PbSe QDs.

Bibliography

[1] U.S. Energy Information Administration, International Energy Outlook 2013, http://www.eia.gov/forecasts/ieo/.

[2] European Commission, World Energy Technology Outlook - 2050, 2006, http://ec.europa.eu/research/energy/pdf/weto-h2_en.pdf.

[3] Owen, N. A.; Inderwildi, O. R.; King, D. A.; Energy Policy 38 (2010) 4743-4749.

[4] Becquerel, A. E.; Comptes Rendus de l'Academie des Sciences, vol. 9, 561-567 (1839).

[5] Day, R. E.; Adams, W. G.; Proc. R. Soc. Lond., 1876, 25, 113-117.

[6] Solar energy conversion, G. W. Crabtree, N. S. Lewis, Physics Today, 60(3), 37-40 (March 2007).

[7] Goodrich, A. C.; Powell, D. M.; James, T. L.; Woodhouse, M.; Buonassisi, T.; Energy Environ. Sci., 2013, 6, 2811-2821.

[8] Shockley, W.; Queisser, H. J.; J. Appl. Phys. 32, 510 (1961).

[9] O'Regan, B.; Grätzel, M.; Nature 1991, 353, 737.

[10] Hagfeldt, A.; Boschloo, G.; Sun, L.; Kloo, L.; Pettersson, H.; Chem. Rev., 2010, 100 (11), 6595-6663.

[11] Kalyanasundram, K.; Dye-Sensitized Solar Cells, EPFL Press, 2010, ISBN: 978-2-940222-36-0.

[12] Burschka, J.; Pellet, N.; Soo-Jin M.; Humphry-Baker, R.; Gao, P.; Nazeeruddin, M. K.; Grätzel, M.; Nature, 499(7458), 316-319.

[13] Tauc, J.; J. Phys. Chem. Solids, 219 (1959).

[14] Vavilov, V. S.; J. Phys. Chem. Solids 8, 223 (1959).

[15] Ekimov, A. I.; Onushchenko, A. A.; JETP Lett., Vol 34, 1981, 345-349.

[16] Rossetti, R.; Nakahara, S.; Brus, L. E.; J. Chem. Phys. Vol. 79, 1983, 1086-1088.

[17] Schaller, R. D.; Klimov, V. I.; Phys. Rev. Lett. 92, 186601 (2004).

[18] Murphy, J. E.; Beard, M. C.; Norman, A. G.; Ahrenkiel, S. P.; Johnson, J. C.; Pingrong, Y.; Mićić, O. I.; Ellingson, R. J.; Nozik, A. J.; J. Am. Chem. Soc. 2006, 128, 3241-3247.

[19] Nozik, A. J.; Chemical Physics Letters, 457 (2008) 3-11.

[20] Michalet, X.; Pinaud, F. F.; Bentolila, L. A.; Tsay, J. M.; Doose, S.; Li, J. J.; Sundaresan, G.; Wu, A. M.; Gambhir, S. S.; Weiss, S.; Science, 307, 5709, 538-544 (2005).

[21] Shuhendler, A. J.; Prasad, P.; Chan, H. C.; Gordijo, C. R.; Soroushian, B.; Kolios, M.; Yu, K.; O'Brien, P. J.; Rauth, A. M.; Wu, X. Y.; ACS Nano, Vol. 5, No. 3, 1958-1966, 2011.

[22] Ladd, T. D.; Jelezko, F.; Laflamme, R.; Nakamura, Y.; Monroe, C.; O'Brien, J. L.; Nature 464, 45-53 (2010).

[23] Shirasaki, Y.; Supran, G. J.; Bawendi, M. G.; Bulović, V.; Nature Photonics, 7, 13-23 (2013).

[24] Murray, C. B.; Norris, D. J.; Bawendi, M. G.; J. Am. Chem. Soc. 115, 8706-8715 (1993).

[25] Greenham, N. C.; Peng, X.; Alivisatos, A. P.; Phys. Rev. B 1996, 54, 17628.

[26] Zaban, A.; Mićić; Gregg, B. A.; Nozik, A. J.; Langmuir, 1998, 14 (12) 3153-3156.

[27] Zhang, H.; Cheng, K.; Hou, Y. M.; Fang, Z.; Pan, Z. X.; Wu, W. J.; Hua, J. L.; Zhong, X. H.; Chem. Commun. 2012, 48, 11235.

[28] Ip, A. H.; Thon, S. M.; Hoogland, S.; Voznyy, O.; Zhitomirsky, D.; Debnath, R.; Levina, L.; Rollny, L. R.; Carey, G. H.; Fischer, A.; Kemp, K. W.; Kramer, I. J.; Ning, Z.; Labelle, A. J., Chou, K. W.; Amassian, A.; Sargent, E. H.; Nature Nanotechnology, Vol 7, September 2012, 577-582.

[29] Sykora, M.; Koposov, A. Y.; McGuire, J. A.; Schulze, R. K.; Tretiak, O.; Pietryga, J. M.; Klimov, V. I.; ACS Nano 2010, Vol. 4, No. 4, 2021-2034.

[30] Beard, M. C.; J. Phys. Chem. Lett. 2011, 2, 1282-1288.

[31] Arakawa, Y.; Sakaki, H.; Appl. Phys. Lett. 40, 939 (1982).

[32] Asada, M.; Miyamoto, Y.; Suematsu, Y.; IEEE Journal of Quantum Electronics, Vol. QE-22, No. 9, 1986, 1915-1921.

[33] Tansu, N.; Yeh, J-Y.; Mawst, L. J., App. Phys. Lett. 82, 23, 4038-4040, 2003.

[34] "'Quantum Dot and Quantum Dot Display (QLED): Market Shares, Strategies, and Forecasts, Worldwide, Nanotechnology, 2013 to 2019."' WinterGreen Research, Inc. 2013.

[35] Sukhovatkin, V.; Hinds, S.; Brzozowski, L. Sargent, E. H.; Science, 324 (5934), 1542-1544 (2009).

[36] Colvin, V. L.; Schlamp, M. C.; Alivisatos, A. P.; Nature, 370, 354-357 (1994).

[37] Stouwdam, J. W.; Janssen, R. A. J.; J. Mater. Chem. 18, 1889-1894 (2008).

[38] Bourzac, K.; Nature, 493, 283 (2013).

[39] Grimme, S.; Antony, J.; Ehrlich, S.; Krieg, H.; J. Chem. Phys. 132, 154104 (2010).

[40] Chan, M. K. Y; Ceder, G.; Phys. Rev. Lett 105, 196403 (2010).

[41] Koopmans, T.; Physica, 1933, 1, 104.

[42] Janak, J. F.; Phys. Rev. B 178, 18, 7165.

[43] Stowasser, R.; Hoffmann, R.; J. Am. Chem. Soc., Vol 121, No. 14, 1999.

[44] Hamel, S.; Duffy, P.; Casida, M. E.; Salahub, D. R.; J. Electron Spectrosc. Relat. Phenom. 2002, 123, 345.

[45] Zhang, G.; Musgrave, C. B.; J. Phys. Chem. A 2007, 111, 1554-1561.

[46] Boys, S. F.; Bernardi, F.; Mol. Phys. 1970, 19, 553.

[47] Haram, S. K.; Kshirsagar, A.; Gujarathi, Y. D.; Ingole, P. P.; Nene, O. A.; Markad, G. B.; Nanavati, S. P.; J. Phys. Chem. C. 2011, 115, 6243-6249.

[48] Bisri, S. Z.; Degoli, E.; Spallanzani, N.; Krishnan, G.; Kooi, B. J.; Ghica, C.; Yarema, M.; Heiss, W.; Pulci, O.; Ossicini, S.; Loi, M. A.; Adv. Mater. 2014, DOI: 10.1002/adma.201400660.

[49] Corà, F.; Alfredsson, M.; Middlemiss, D. S.; Mackrodt, W. C.; Dovesi, R.; Orlando, R.; (2004) Density Functional Theory in Inorganic Chemistry (pp. 171-232). Heidelberg Springer-Verlag.

[50] Ma, W.; Swisher, S. L.; Ewers, T.; Ferry, V. E.; Atwater, H. A.; Alivisatos, A. P.; ACS Nano, 2011, 5 (10), 8140-8147.

[51] Efros, A. L., Efros, A. L.; Sov. Phys. Semicond. 16 (7), 772-775 (1982).

[52] Isborn, C. M.; Prezhdo, O. V.; J. Phys. Chem. C Lett. 2009, 113, 29, 12617-12621.

[53] Isborn, C. M.; Kilina, S. V.; Li, X.; Prezhdo, O. V.; J. Phys. Chem. C Lett. 2008, 112, 47, 18291-18294.

[54] Kramer, I. J.; Sargent, E. H.; Chem. Rev. 2014, 114, 863-882.

[55] Kramer, I. J.; Sargent, E. H.; ACS Nano, 2011, 5 (11), 8506-8514.

[56] Sashchiuk, A.; Langof, L.; Chaim, R.; Lifshitz, E.; Journal of Crystal Growth 240 (2002) 431-438.

[57] Law, M.; Luther, J. M; Qing, S.; Hughes, B. K.; Perkins, C. L.; Nozik, A. J.; J. Am. Chem. Soc. 2008, 130, 5974-5985.

[58] Li, H.; Chen, D.; Li, L.; Tang, F.; Zhang, L.; Ren, J.; CrystEngComm, 2010, 12, 1127-1133.

[59] Zeng, Q.; Shi, J.; Jiang, G.; Yang, M.; Wang, F.; Chen, J.; J. Chem. Phys 139, 094305 (2013).

[60] Akhtar, J.; Malik, M. A.; O'Brien, P.; Revaprasadu, N.; Materials Letters 77 (2012) 78-81.

[61] In C. B.; Sang I. S.; Pramanik, N. C.; Jana, S.; Mi A. L.; Boek, Y. A.; Chang, J. L.; Yong, J. J.; Journal of Colloid and Interface Science 310 (2007), 163-166.

[62] Trinidade, T.; Monteiro, O. A.; O'Brien, P.; Montevalli, M.; Polyhedron 18, (1999) 1171-1175.

[63] Moreels, I.; Fritzinger, B.; Martins, J. C.; Hens, Z.; J. Am. Chem. Soc. 2008, 130, 15081-15086.

[64] Boys, S.; Bernardi, F.; Mol. Phys. 1970, 19, 553.

[65] Argeri, M.; Fraccarollo, A.; Grassi, F.; Marchese, L.; Cossi, M.; J. Phys. Chem. C 2011, 115, 11382-11389.

[66] Fang, C.; van Huis, M. A.; Vanmaekelbergh, D.; Zandbergen, H. W.; ACS Nano, Vol. 4, No. 1, 211-218, 2010.

[67] Moreels, I.; Lambert, K.; De Muynck, D.; Vanhaecke, F.; Poelman, D.; Martins, J. C.; Allan, G.; Hens, Z.; Chem. Mater. 2007, 19, 6101-6106.

[68] Primera-Pedrozo, O. M.; Arslan, Z.; Rauslev, B.; Leszczynski, J.; Nanoscale, 2012, 4, 1312.

[69] Tuinenga, C.; Jasinski, J.; Iwamoto, T.; Chikan, V.; ACS Nano Vol. 2, No. 7, 1411-1421, 2008.

[70] Roy, S.; Tuinenga, C.; Fungura, F.; Dagtepe, P.; Chikan, V.; J. Phys. Chem. C 2009, 113, 13008-13015.

[71] Mocatta, D.; Cohen, G.; Schattner, J.; Millo, O.; Rabani, E.; Banin, U.; Science 332, 77 (2011).

[72] Pradhan, N.; Sarma, D. D.; J. Phys. Chem. Lett. 2011, 2, 2818-2826.

[73] Santra, P. K.; Kamat, P. V.; J. Am. Chem. Soc. 2012, 134, 2508-2511.

[74] Dovesi, R.; Orlando, R.; Civalleri, B.; Roetti, C.; Saunders, V. R.; Zicovich-Wilson, C. M.; Z. Kristallogr. 2005, 220, 571-573.

[75] Dovesi, R.; Saunders, V. R.; Roetti, C.; Orlando, R.; Zicovich-Wilson, C. M.; Pascale, F.; Civalleri, B.; Doll, K.; Harrison, N. M.; Bush, I. J.; D'Arco, P.; Llunell, M.; CRYSTAL09 User's Manual. University of Torino: Torino, 2009.

[76] Hay, P. J.; Wadt, W. R., J. Chem. Phys. 82 (1985) 270.

[77] Wadt, W. R.; Hay, P. J., J. Chem. Phys. 82 (1985) 284.

[78] Hay, P. J.; Wadt, W. R., J. Chem. Phys. 82(1985) 299.

[79] Hariharan, P. C.; Pople, J. A., Theor. Chim. Acta 28 (1973) 213; Dunning, T. H., Jr., J. Chem. Phys. 90 (1989) 1007.

[80] Dunning, T.; J. Chem. Phys. 1989, 90, 1007-1023.

[81] Becke, A. D.; Phys. Rev. A. 1988, 38, 3098-3100.

[82] Lee, C.; Yang, W.; Parr, R. G.; Phys. Rev. B 1988, 37, 785.

[83] Becke, A. D., Phys. Rev. B 38 (1988) 3098; Becke, A. D., J. Chem. Phys. 98(1993) 1372.

[84] Ahlrichs, R.; Bär, M.; Häser, M.; Horn, H.; Kölmen, C., Chem. Phys. Lett. 162 (1989) 165; Arnim, M.; Ahlrichs, R., J. Chem. Phys. 111 (1999) 9183.

[85] Frisch, M. J.; Trucks, G. W.; Schlegel, H. B.; Scuseria, G. E.; Robb, M. A.; Cheeseman, J. R.; Scalmani, G.; Barone, V.; Mennucci, B.; Petersson, G. A.; Nakatsuji, H.; Caricato, M.; Li, X.; Hratchian, H. P.; Izmaylov, A. F.; Bloino, J.; Zheng, G.; Sonnenberg, J. L.; Hada, M.; Ehara, M.; Toyota, K.; Fukuda, R.; Hasegawa, J.; Ishida, M.; Nakajima, T.; Honda, Y.; Kitao, O.; Nakai, H.; Vreven, T.; Montgomery, J. A., Jr.; Peralta, J. E.; Ogliaro, F.; Bearpark, M.; Heyd, J. J.; Brothers, E.; Kudin, K. N.; Staroverov, V. N.; Kobayashi, R.; Normand, J.; Raghavachari, K.; Rendell, A.; Burant, J. C.; Iyengar, S. S.; Tomasi, J.; Cossi, M.; Rega, N.; Millam, N. J.; Klene, M.; Knox, J. E.; Cross, J. B.; Bakken, V.; Adamo, C.; Jaramillo, J.; Gomperts, R.; Stratmann, R. E.; Yazyev, O.; Austin, A. J.; Cammi, R.; Pomelli, C.; Ochterski, J. W.; Martin, R. L.; Morokuma, K.; Zakrzewski, V. G.; Voth, G. A.; Salvador, P.; Dannenberg, J. J.; Dapprich, S.; Daniels, A. D.; Farkas, Ö.; Foresman, J. B.; Ortiz, J. V.; Cioslowski, J.; Fox, D. J. Gaussian, Inc., Wallingford CT, 2009.

[86] Grimme, S.; J. Comput. Chem. 2006, 27, 1787-1799.

[87] Check, C. E.; Faust, T. O.; Bailey, J. M.; Wright, B. J.; Gilbert, T. M.; Sunderlin, L. S.; J. Phys. Chem. A 2001, 105, 8111-8116.

[88] Vazquez-Mayagoitia, A.; Vargas, R.; Nichols, J. A.; Fuentealba, P.; Garza, J., Chem. Phys. Lett. 419 (2006) 207.

[89] von Oertzen, G. U.; Jones, R. T.; Gerson, A. R.; Phys. Chem. Minerals 32 (2005), 255.

[90] Gokarna, A.; Jun, K. W.; Khanna, P. K.; Baeg, J. O.; Seok, S. I.; Bull. Korean Chem. Soc. 2005, Vol. 26, No. 11, 1803-1806.

[91] Houtepen, A. J.; Koole, R.; Vanmaekelbergh, D.; Meeldijk, J.; Hickey, S. G.; J. Am. Chem. Soc. 2006, 128, 6792-6793.

[92] Britt, D. K.; Yoon, Y.; Ercius, P.; Ewers, T. D.; Alivisatos, A. P.; Chem. Mater., 2013, 25 (12), pp. 2544-2548.

[93] Rojas-Chavez, H.; Reyes-Carmona, F.; Acimovičovà, M.; Daneu, N.; Jaramillo-Vigueras, D.; J. Nanopart. Res. (2012) 14:897.